Charged Bis-Cyclometalated Iridium(III) Complexes with Carbene-Based Ancillary Ligands

Filippo Monti,[†] Florian Kessler,[§] Manuel Delgado,[‡] Julien Frey,[§] Federico Bazzanini,[†] Gianluca Accorsi,[†] Nicola Armaroli,*[,†] Henk J. Bolink,[‡] Enrique Ortí,*[,‡] Rosario Scopelliti,[§] Md. Khaja Nazeeruddin,[§] and Etienne Baranoff*[,⊥]

[†]Istituto per la Sintesi Organica e la Fotoreattività, Consiglio Nazionale delle Ricerche, Via P. Gobetti 101, 40129 Bologna, Italy

[‡]Instituto de Ciencia Molecular, Universidad de Valencia, 46980 Paterna, Spain

[§]Laboratory of Photonics and Interfaces, Institute of Chemical Sciences and Engineering, École Polytechnique Fédérale de Lausanne, CH-1015 Lausanne, Switzerland

[⊥]School of Chemistry, University of Birmingham, Edgbaston, Birmingham B15 2TT, U.K.

Ⓢ *Supporting Information*

ABSTRACT: Charged cyclometalated (C^N) iridium(III) complexes with carbene-based ancillary ligands are a promising family of deep-blue phosphorescent compounds. Their emission properties are controlled primarily by the main C^N ligands, in contrast to the classical design of charged complexes where N^N ancillary ligands with low-energy π^* orbitals, such as 2,2'-bipyridine, are generally used for this purpose. Herein we report two series of charged iridium complexes with various carbene-based ancillary ligands. In the first series the C^N ligand is 2-phenylpyridine, whereas in the second one it is 2-(2,4-difluorophenyl)-pyridine. One bis-carbene (:C^C:) and four different pyridine−carbene (N^C:) chelators are used as bidentate ancillary ligands in each series. Synthesis, X-ray crystal structures, and photophysical and electrochemical properties of the two series of complexes are described. At room temperature, the :C^C: complexes show much larger photoluminescence quantum yields (Φ_{PL}) of ca. 30%, compared to the N^C: analogues (around 1%). On the contrary, all of the investigated complexes are bright emitters in the solid state both at room temperature (1% poly(methyl methacrylate) matrix, Φ_{PL} 30−60%) and at 77 K. Density functional theory calculations are used to rationalize the differences in the photophysical behavior observed upon change of the ancillary ligands. The N^C:-type complexes possess a low-lying triplet metal-centered (^{3}MC) state mainly deactivating the excited state through nonradiative processes; in contrast, no such state is present for the :C^C: analogues. This finding is supported by temperature-dependent excited-state lifetime measurements made on representative N^C: and :C^C: complexes.
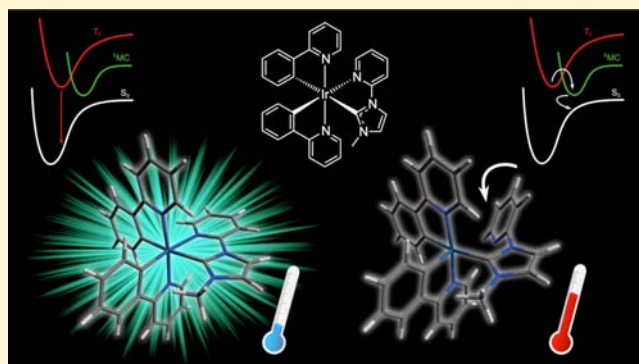
INTRODUCTION

Octahedral iridium(III) complexes equipped with cyclometalating (C^N) ligands are typically robust compounds exhibiting relatively long-lived (microsecond time scale) and often highly luminescent triplet excited states.[1] Their photophysical and electrochemical properties are attracting considerable interest for several applications such as catalysts for artificial photosynthesis, nonlinear optics, photodynamic therapy, photovoltaic cells, and luminescent sensors.[2] These emerging applications are further extending the use of Ir(III) complexes beyond the established areas of organic light-emitting diodes (OLEDs) and light-emitting electrochemical cells (LECs), where they serve as the ultimate triplet emitters because, by ligand design, their luminescence hue can be tuned all the way from blue to red.[3−5] The development of stable deep-blue Ir-based emitters, however, is a rather challenging task.[3,4] In the case of neutral iridium(III) complexes for OLEDs, the deep-blue emission was achieved by using ligands with high triplet energy levels such as carbene- or pyrazole-based chelators.[6,7] In the case of cationic phosphorescent emitters for LECs, high-energy emission was usually obtained with monodentate ligands,[8] recently reaching emission band onset as low as 400 nm,[9] or with bidentate ligands bearing a methylene bridge.[10,11] In the former case, monodentate ligands are prone to decoordination; in the latter case, a limited stability of the material is expected because the delocalization between the two aromatic rings is broken, and a six-membered metallacycle with the iridium center is formed. To improve the stability of chelation, bidentate ancillary ligands forming a five-membered metallacycle are preferable.

Typical examples of charged bis-C^N iridium(III) complexes are based on neutral N^N ancillary ligands (e.g., bipyridine,[12−19] phenanthroline,[20] pyridine−pyrazole,[21] pyridine−imidazole,[22] pyridine−triazole,[23] and pyridine−tetrazole[24]) that form five-membered metallacycles with the metal center. In these complexes, the emission typically originates from a metal-to-ligand charge transfer (MLCT) triplet state mainly involving the iridium ion and the N^N ancillary ligand. Deeper-blue emission can be obtained by using N^N ligands that have a higher-lying lowest-unoccupied molecular orbital (LUMO) than bipyridine, by stabilizing the highest-occupied molecular orbital (HOMO) through introduction of fluorine electron-withdrawing groups on the orthometalated phenyl ring, or both.[21,22] Only recently, we reported a strategy based on a neutral pyridine−carbene (N^C:) ancillary ligand forming a five-membered ring with the iridium center.[25] Interestingly, the very high energy of the LUMO centered on the N^C: ligand leads to a predominantly ligand-centered (LC) emission from the C^N ligands. Tuning the emission maximum becomes straightforward by modifying the chemical structure of the C^N ligands, by modifying the substituents of the C^N ligands, or both, easily leading to the deep-blue emission with band onsets as low as 380 nm.[25]

Although the use of carbene-based ancillary ligands has opened new avenues for the design of charged complexes that emit deep-blue light, the resulting materials display low emission quantum yields compared to standard neutral iridium-based emitters.[11,25,26] To understand the reasons behind this limitation, we prepared two series of complexes with one bis-carbene (:C^C:) and four different N^C: chelators as bidentate ancillary ligands. We used 2-phenylpyridine (ppy) and 2-(2,4-difluorophenyl)pyridine (diFppy) as the main C^N ligands for each series. A full photophysical and electrochemical characterization of the two series of complexes was performed, and the results are rationalized with the help of density functional theory (DFT) calculations. In contrast to the complexes based on the N^C: ancillary ligands, no low-energy triplet metal-centered (^3MC) state was localized for the :C^C: complexes, which explains the larger values observed for the photoluminescence quantum yields (Φ_{PL}) of such complexes.

■ EXPERIMENTAL PROCEDURES

Materials and Methods. L1, L5, 1-(4-methyl-2-pyridyl)-benzimidazole, $[Ir(ppy)_2(\mu\text{-}Cl)]_2$, $[Ir(diFppy)_2(\mu\text{-}Cl)]_2$, **1a**,[25] **1b**,[25] and **5b**[11] were synthesized as previously reported. The syntheses of **4a** and **4b** were reported in ref 26. All the commercial materials and solvents were of reagent quality and were used as received. The ^1H and ^{13}C NMR spectra were recorded with the use of a Bruker AV 400 MHz spectrometer. The chemical shifts δ (in ppm) are referenced to the residual solvent peaks. For ^1H NMR, the solvents included $CDCl_3$ (7.24 ppm), acetone-d_6 (2.05 ppm), dimethyl sulfoxide (DMSO)-d_6 (2.50 ppm); for ^{13}C NMR, the solvent was $CDCl_3$ (77.0 ppm). The ^{19}F and ^{31}P NMR spectra were recorded with the use of a Bruker AV 200 MHz spectrometer. The coupling constants are expressed in hertz (Hz). The high-resolution mass spectra (HRMS) were obtained with a Waters Q-TOF-MS instrument using electrospray ionization (ESI). The elemental analyses were performed by Dr. E. Solari, Service for Elemental Analysis, Institute of Chemical Sciences and Engineering (ISIC EPFL). The voltammetric measurements employed a personal computer-controlled AutoLab PSTAT10 electrochemical workstation and were carried out in an Ar-filled glovebox in which $[O_2]$ and $[H_2O]$ < 1 ppm. Cyclic voltammetry (CV) and differential pulse voltammetry (DPV) techniques were used to estimate the redox potentials. The DPV was used to support the CV to have a better estimate of the electrochemical potentials when the systems showed behavior close to

irreversibility; that is, one of the two peaks in the CV was not well-defined. The DPVs were carried out with sweeps from negative to positive potentials, and the mean values were calculated. The CVs were obtained at a scan rate of 1 and 0.1 V s^{-1}. The DPVs were obtained at a modulation potential of 50 mV, a step potential of 10 mV, a modulation time of 50 ms, and an interval time of 100 ms. The measurements were carried out using 0.1 M tetrabutylammonium hexafluorophosphate (TBAPF$_6$) as the supporting electrolyte in acetonitrile (MeCN). Glassy carbon, platinum plate, and platinum wire were used as working, counter, and quasi-reference electrodes, respectively. At the end of each measurement, ferrocene was added as an internal reference. The data collections for the X-ray crystal structures were performed on a Bruker APEX II CCD at low temperature [100(2) K] with the use of Mo Kα radiation having kappa geometry. All the data sets were reduced by means of EvalCCD[27] and then corrected for absorption.[28] The solutions and refinements were performed by SHELX.[29] The crystal structures were refined using the full-matrix least-squares method on the basis of F^2 with all the non-hydrogen atoms anisotropically defined. The hydrogen atoms were placed in calculated positions by means of the "riding" model.

Photophysical Measurements. The spectroscopic investigations were carried out in CH_3CN and CH_2Cl_2 (Carlo Erba, spectrofluorimetric grade) used without further purification. The absorption spectra were recorded with a Perkin−Elmer Lambda 950 spectrophotometer. For the photoluminescence experiments, the samples were placed in fluorimetric Suprasil quartz cuvettes (1 cm) and were purged of oxygen by bubbling with argon. The uncorrected emission spectra were obtained with an Edinburgh FLS920 spectrometer equipped with a Peltier-cooled Hamamatsu R928 photomultiplier tube (PMT) (185−850 nm). An Edinburgh Xe900 450 W xenon arc lamp was used as the excitation light source. The corrected spectra were obtained via a calibration curve supplied with the instrument. The Φ_{PL} in solution were obtained from the corrected spectra on a wavelength scale (nm) and measured according to the approach described by Demas and Crosby[30] in which an air-equilibrated $[Ru(bpy)_3][Cl]_2$ water solution ($\Phi_{PL} = 0.028$)[31] or an air-equilibrated solution of quinine sulfate in 1 N H_2SO_4 ($\Phi_{PL} = 0.546$)[32] was used as a standard. The emission lifetimes (τ) in the nanosecond and microsecond ranges were measured through the time-correlated single photon counting (TCSPC) technique with the use of the same Edinburgh Instruments FLS920 spectrometer equipped with a laser diode as the excitation source (1 MHz; λ_{exc} = 407 nm; 200 ps time resolution after deconvolution) and the aforementioned PMT as the detector. The analysis of the luminescence decay profiles was accomplished with a decay-analysis software provided by the manufacturer, and the quality of the fit was assessed with the χ^2 value close to unity and with the residuals regularly distributed along the time axis. To record the 77 K luminescence spectra, the samples were put in quartz tubes (2 mm inner diameter) and inserted into a special quartz Dewar flask filled with liquid nitrogen. The solid samples were prepared by following two different procedures: the poly(methyl methacrylate) (PMMA) films containing 1 wt% of the complex were drop-cast from dichloromethane solutions; the neat films of the complexes were spin-coated from acetonitrile solutions. The thickness of the films was not controlled. The solid-state Φ_{PL} values were calculated with the use of corrected emission spectra obtained by an Edinburgh FLS920 spectrometer equipped with a barium sulfate-coated integrating sphere (diameter of 4 in.) and by the procedure described by De Mello et al.[33] For temperature-dependent measurements, all the samples were dissolved in butyronitrile, bubbled with argon for 15 min, and sealed in a 1 cm diameter vial. This was placed inside an Oxford Optistat DN variable-temperature liquid-nitrogen cryostat (operating range: 77−500 K) equipped with an ITC5035 temperature controller, interfaced with the aforementioned Edinburgh FLS920 spectrometer. The experimental uncertainties are estimated to be ±8% for τ determinations, ±20% for Φ_{PL}, and ±2 and ±5 nm for absorption and emission peaks, respectively.

Computational Details. The DFT calculations were carried out with the C.01 revision of the Gaussian 09 program package[34] using Becke's three-parameter B3LYP exchange-correlation functional[35,36]

together with the 6-31G** basis set for C, H, F, and N,[37] and the "double-ζ" quality LANL2DZ basis set for the Ir element.[38] The geometries of the singlet ground state (S_0) and the lowest-energy triplet states were fully optimized without imposing any symmetry restriction. The geometries of the triplet states were calculated at the spin-unrestricted UB3LYP level with a spin multiplicity of 3. With the use of frequency calculations, all the optimized structures including both the electronic ground state and the excited triplet states were characterized as energy minima. All the calculations were performed in the presence of the solvent (acetonitrile). The solvent effects were considered within the self-consistent reaction field (SCRF) theory using the solvation model density (SMD) keyword that performs a polarized continuum model (PCM)[39−41] calculation with the use of the solvation model of Thrular and co-workers.[42] The SMD solvation model is based on the polarized continuous quantum chemical charge density of the solute. The time-dependent DFT (TD-DFT) calculations of the lowest-lying 40 triplets were performed in the presence of the solvent at the minimum-energy geometry optimized for S_0.

3-Hexyl-1-(4-methyl-2-pyridyl)benzimidazolium Bromide (L2). 1-Bromohexane (0.91 mL, 6.5 mmol, 2 equiv) was added to a solution of 1-(4-methyl-2-pyridyl)benzimidazole[43] (0.68 g, 3.25 mmol, 1 equiv) in 20 mL of toluene, and the mixture was heated overnight at 100 °C. After the mixture was cooled to ambient temperature, the white precipitate was collected on a glass frit, washed with 5 mL of toluene, and dried in a vacuum. The filtrate was concentrated, 1 equiv of 1-bromohexane was added, and the procedure was repeated to increase the yield. The product was obtained as a white powder (0.49 g, 1.3 mmol, 40%). ^{1}H NMR (400 MHz, acetone-d_6): δ 12.03 (s, 1H, NCHN), 8.68−8.64 (m, 1H, ArH), 8.45 (d, $^3J_{HH}$ = 5.0 Hz, 1H, ArH), 7.81−7.79 (m, 1H, ArH), 7.68−7.64 (m, 2H, ArH), 7.38−7.37 (m, 1H, ArH), 7.28 (d, $^3J_{HH}$ = 5.0 Hz, 1H, ArH), 4.81 (t, $^3J_{HH}$ = 7.5 Hz, 2H, NCH$_2$), 2.53 (s, 3H, ArCH$_3$), 2.14−2.08 (m, 2H, CH$_2$), 1.48−1.40 (m, 2H, CH$_2$), 1.35−1.21 (m, 4H, CH$_2$CH$_2$), 0.80 (t, $^3J_{HH}$ = 7.1 Hz, 3H, CH$_3$). ^{13}C NMR (100 MHz, CDCl$_3$): δ 153.0 (ArC), 148.7 (ArC), 148.2 (ArC), 141.3 (ArC), 131.8 (ArC), 130.3 (ArC), 128.3 (ArC), 127.9 (ArC), 126.0 (ArC), 117.9 (ArC), 113.0 (ArC), 48.3 (NCH$_2$), 31.3 (CH$_2$), 29.7 (CH$_2$), 26.3 (CH$_2$), 22.5 (ArCH$_3$), 21.5 (CH$_2$), 14.1 (CH$_2$). HRMS (ESI-TOF) m/z (%): calcd. 294.1970; found 294.1962 (100) [(M − Br)$^+$]. Anal. Calc. for C$_{19}$H$_{24}$BrN$_3$ (373.12): C 60.97, H 6.46, N 11.23. Found: C 60.65, H 6.54, N 10.89.

3-Methyl-1-(4-methyl-2-pyridyl)imidazolium Iodide (L3). Imidazole (2.04 g, 30 mmol, 1.5 equiv), KOH (2.24 g, 40 mmol, 2 equiv), and Cu$_2$O (286 mg, 2.0 mmol, 0.1 equiv) were added to a flask. The flask was then sealed with a septum, evacuated, and backfilled with nitrogen. DMSO (30 mL) and 2-bromo-4-methylpyridine (2.23 mL, 20 mmol, 1 equiv) were added to the flask, and the mixture was heated at 120 °C for 36 h. After the mixture was cooled to ambient temperature, water was added, and the aqueous phase was extracted with CH$_2$Cl$_2$ (3 × 75 mL). The combined organic layers were dried over MgSO$_4$. The crude product was purified by column chromatography over a short plug of silica with EtOAc as eluent. The residue was dissolved in toluene, methyl iodide (2.50 mL, 40 mmol, 2 equiv) was added, and the mixture was heated overnight at 80 °C. After the mixture was cooled to ambient temperature, the off-white precipitate was collected on a glass frit, washed with 50 mL of toluene, and dried in a vacuum. The product obtained was a white powder (4.70 g, 15.6 mmol, 78% yield over two steps). ^{1}H NMR (400 MHz, CDCl$_3$): δ 11.06 (s, 1H, NCHN), 8.38 (d, $^3J_{HH}$ = 5.1 Hz, 1H, ArH), 8.31 (br s, 1H, ArH), 8.29 (t, $^3J_{HH}$ = 1.8 Hz, 1H, ArH), 7.67 (t, $^3J_{HH}$ = 1.8 Hz, 1H, ArH), 7.28 (d, $^3J_{HH}$ = 4.6 Hz, 1H, ArH), 4.32 (s, 3H, NCH$_3$), 2.57 (s, 3H, ArCH$_3$). ^{13}C NMR (100 MHz, CDCl$_3$): δ 152.3 (ArC), 148.5 (ArC), 145.6 (ArC), 134.3 (ArC), 126.0 (ArC), 124.6 (ArC), 118.8 (ArC), 114.8 (ArC), 37.6 (NCH$_3$), 21.0 (ArCH$_3$). HRMS (ESI-TOF) m/z (%): calcd. 174.1031; found 174.1033 (100) [(M − I)$^+$]. Anal. Calc. for C$_{10}$H$_{12}$IN$_3$ (301.01): C 39.89, H 4.02, N 13.95. Found: C 39.46, H 4.10, N 13.75.

3-Methyl-1-(2-pyridyl)imidazolium Iodide (L4). Imidazole (0.51 g, 7.5 mmol, 1.5 equiv), KOH (0.56 g, 10 mmol, 2 equiv), and Cu$_2$O (72 mg, 0.5 mmol, 0.1 equiv) were added to a flask. The

flask was then sealed with septum, evacuated, and backfilled with nitrogen. DMSO (10 mL) and 2-bromopyridine (0.48 mL, 5 mmol, 1 equiv) were added to the flask, and the mixture was heated at 120 °C for 36 h. After the mixture was cooled to ambient temperature, water was added, and the aqueous phase was extracted with CH$_2$Cl$_2$ (3 × 25 mL). The combined organic layers were dried over MgSO$_4$. The crude product was purified by column chromatography over a short plug of silica with EtOAc as eluent. 1-(2-Pyridyl)imidazole was obtained as a yellow oil (0.68g, 4.7 mmol, 94%). The oil was dissolved in toluene, treated with methyl iodide (0.59 mL, 9.4 mmol, 2 equiv), and heated overnight at 80 °C. After the mixture was cooled to ambient temperature, the white precipitate was collected on a glass frit, washed with 20 mL of toluene, and dried in a vacuum. The product obtained was a white powder (0.82 g, 2.9 mmol, 61%). ^{1}H NMR (400 MHz, CDCl$_3$): δ 8.50 (d, $^3J_{HH}$ = 4.8 Hz, 1H, ArH), 8.36 (d, $^3J_{HH}$ = 8.3 Hz, 1H, ArH), 8.25 (t, $^3J_{HH}$ = 1.7 Hz, 1H, ArH), 7.88 (t, $^3J_{HH}$ = 7.9 Hz, 1H, ArH), 7.61 (br s, 1H, ArH), 7.47−7.44 (m, 1H, ArH), 4.29 (s, 3H, NCH$_3$) (the signal for NCHN was not observed). ^{13}C NMR (100 MHz, CDCl$_3$): δ 149.4 (ArC), 146.0 (ArC), 140.7 (ArC), 135.3 (ArC), 125.5 (ArC), 124.5 (ArC), 119.1 (ArC), 115.0 (ArC), 37.9 (NCH$_3$). HRMS (ESI-TOF) m/z (%): calcd. 160.0875; found 160.0880 (100) [(M − I)$^+$]. Anal. Calc. for C$_9$H$_{10}$IN$_3$ (286.99): C 37.65, H 3.51, N 14.64. Found: C 37.33, H 3.57, N 14.61.

[Ir(ppy)$_2$(L2)]PF$_6$ (2a). A solution of L2 (75 mg, 0.200 mmol, 2.1 equiv), silver(I) oxide (26 mg, 0.114 mmol, 1.2 equiv), and [Ir(ppy)$_2$(μ-Cl)]$_2$ (102 mg, 0.095 mmol, 0.5 equiv) in 1,2-dichloroethane was heated to reflux (95 °C) overnight. After cooling to ambient temperature, the mixture was filtered through Celite to remove silver residues. The Celite was washed with CH$_2$Cl$_2$, and the solvent was removed in vacuo. The residue was dissolved in 20 mL of CH$_2$Cl$_2$ and extracted three times with an aqueous KPF$_6$ solution (55 mg of KPF$_6$ in 40 mL of water per cycle). The combined organic layers were washed with water, dried over MgSO$_4$, and concentrated in vacuo. The crude product was purified by column chromatography on silica gel using CH$_2$Cl$_2$ and then CH$_2$Cl$_2$/acetone (4:1 v/v) as solvent. First 145 mg (0.145 mmol, 81%) of 2a was collected, then 32 mg (0.034 mmol, 18%) of the bromo salt of the iridium complex was collected. After evaporation of the solvent, the pure product obtained was a yellow solid. Yield: 145 mg (0.154 mmol, 81%). ^{1}H NMR (400 MHz, CDCl$_3$): δ 8.35 (d, $^3J_{HH}$ = 8.4 Hz, 1H, ArH), 8.26 (s, 1H, ArH), 7.90 (m, 3H, ArH), 7.75 (bt, $^3J_{HH}$ = 7.9 Hz, 2H, ArH), 7.66 (d, $^3J_{HH}$ = 7.8 Hz, 2H, ArH), 7.63−7.58 (m, 3H, ArH), 7.45 (t, $^3J_{HH}$ = 7.4 Hz, 1H, ArH), 7.39 (d, $^3J_{HH}$ = 8.1 Hz, 1H, ArH), 7.06−7.02 (m, 2H, ArH), 6.99−6.94 (m, 4H, ArH), 6.84 (t, $^3J_{HH}$ = 7.5 Hz, 1H, ArH), 6.39 (d, $^3J_{HH}$ = 7.6 Hz, 1H, ArH), 6.14 (d, $^3J_{HH}$ = 7.4 Hz, 1H, ArH), 3.78 (dtd, $^2J_{HH}$ = 74.8 Hz, $^3J_{HH}$ = 12.5 Hz, $^4J_{HH}$ = 4.8 Hz, 2H, NCH$_2$), 2.66 (s, 3H, ArCH$_3$), 1.52−0.97 (m, 8H CH$_2$CH$_2$CH$_2$CH$_2$), 0.82 (t, $^3J_{HH}$ = 7.3 Hz, 3H, CH$_3$) ppm. ^{31}P NMR (81 MHz, CDCl$_3$): δ −144.5 (sept, $^1J_{PF}$ = 713 Hz, PF$_6$) ppm. ^{19}F NMR (188 MHz, CDCl$_3$): δ −73.4 (d, $^1J_{PF}$ = 712 Hz, PF$_6$) ppm. HRMS (ESI-TOF) m/z (%): calcd. 794.2838; found 794.2780 (100) [(M − PF$_6$)$^+$].

[Ir(diFppy)$_2$(L2)]PF$_6$ (2b). A solution of L2 (79 mg, 0.21 mmol, 2.1 equiv), silver(I) oxide (28 mg, 0.12 mmol, 1.2 equiv), and [Ir(diFppy)$_2$(μ-Cl)]$_2$ (122 mg, 0.1 mmol, 0.5 equiv) in 1,2-dichloroethane was heated to reflux (95 °C) overnight. After cooling to ambient temperature, the mixture was filtered through Celite to remove silver residues. The Celite was washed with CH$_2$Cl$_2$, and the solvent was removed in vacuo. The residue was dissolved in 20 mL of CH$_2$Cl$_2$ and extracted three times with an aqueous KPF$_6$ solution (55 mg of KPF$_6$ in 40 mL of water per cycle). The combined organic layers were washed with water, dried over MgSO$_4$, and concentrated in vacuo. The crude product was purified by column chromatography on silica gel with CH$_2$Cl$_2$ and then CH$_2$Cl$_2$/acetone (9:1 v/v) as solvent. After evaporation of the solvent, the pure product obtained was a yellow solid. Yield: 189 mg (0.187 mmol, 93%). ^{1}H NMR (400 MHz, CDCl$_3$): δ 8.35 (d, $^3J_{HH}$ = 8.5 Hz, 1H, ArH), 8.35 (m, 3H, ArH), 7.94 (d, $^3J_{HH}$ = 5.5 Hz, 1H, ArH), 7.85 (t, $^3J_{HH}$ = 8.1 Hz, 2H, ArH), 7.70−7.63 (m, 3H, ArH), 7.55−7.47 (m, 2H, ArH), 7.19−7.15 (m, 1H, ArH), 7.11 (d, $^3J_{HH}$ = 5.7 Hz, 1H, ArH), 7.08−7.04 (m, 1H, ArH),

6.62−6.53(m, 2H, ArH), 5.83 (dd, $^3J_{HH}$ = 8.5 Hz, $^4J_{HH}$ = 2.3 Hz, 1H, ArH), 5.62 (dd, $^3J_{HH}$ = 7.7 Hz, $^4J_{HH}$ = 2.3 Hz, 1H, ArH), 3.95−3.77 (m, 2H, NCH$_2$), 2.73 (s, 3H, ArCH$_3$), 1.60−1.51 (m, 2H, CH$_2$), 1.26−0.93 (m, 6H CH$_2$CH$_2$CH$_2$), 0.88 (t, $^3J_{HH}$ = 7.4 Hz, 3H, CH$_3$) ppm. ^{13}C NMR (100 MHz, CDCl$_3$): δ 185.9 (NCN), 156.0, 153.8, 153.1, 149.5, 149.1, 139.0, 138.4, 135.1, 131.7, 126.5, 125.6, 125.2, 124.4, 124.2, 124.0, 123.9, 123.6, 123.4, 114.9, 113.8, 111.6, 100.0 (ArC), 48.0 (NCH$_2$), 31.4 (ArCH$_3$), 30.8, 26.3, 22.5, 22.0 (CH$_2$CH$_2$CH$_2$CH$_2$), 13.9 (CH$_3$) ppm. ^{31}P NMR (81 MHz, CDCl$_3$): δ −144.6 (sept, $^1J_{PF}$ = 713 Hz, PF$_6$) ppm. ^{19}F NMR (188 MHz, CDCl$_3$): δ −73.3 (d, $^1J_{PF}$ = 712 Hz, PF$_6$), −105.1 (vq, J = 10.2 Hz, ArF), −106.0 (vq, J = 10.1 Hz, ArF), −107.9 (vt, J = 12.5 Hz, ArF), −108.6 (vt, J = 11.9 Hz, ArF) ppm. HRMS (ESI-TOF) m/z (%): calcd. 866.2460; found 866.2463 (100) [(M − PF$_6$)$^+$].

[Ir(ppy)$_2$(L3)]PF$_6$ (3a). A solution of L3 (63 mg, 0.21 mmol, 2.1 equiv), silver(I) oxide (28 mg, 0.12 mmol, 1.2 equiv), and [Ir(ppy)$_2$(μ-Cl)]$_2$ (107 mg, 0.10 mmol, 0.5 equiv) in 12 mL of 1,2-dichloroethane was heated to reflux (95 °C) overnight. After cooling to ambient temperature, the mixture was filtered through Celite to remove silver residues. The Celite was washed with CH$_2$Cl$_2$, and the solvent was removed in vacuo. The residue was dissolved in 20 mL of CH$_2$Cl$_2$ and extracted three times with an aqueous KPF$_6$ solution (55 mg of KPF$_6$ in 40 mL of water per cycle). The combined organic layers were washed with water, dried over MgSO$_4$, and concentrated in vacuo. The crude product was purified by column chromatography on silica gel with CH$_2$Cl$_2$ and then CH$_2$Cl$_2$/acetone (4:1 v/v) as solvent. After evaporation of the solvent, the pure product obtained was a yellow solid. Yield: 123 mg (0.15 mmol, 75%). ^{1}H NMR (400 MHz, CDCl$_3$): δ 7.97 (d, $^4J_{HH}$ = 2.2 Hz, 1H, ArH), 7.90−7.83 (m, 4H, ArH), 7.75−7.70 (m, 2H, ArH), 7.64 (t, $^3J_{HH}$ = 8.3 Hz, 2H, ArH), 7.49 (t, $^3J_{HH}$ = 5.3 Hz, 2H, ArH), 7.05−6.97 (m, 4H, ArH), 6.94−6.88 (m, 3H, ArH), 6.80 (t, $^3J_{HH}$ = 7.4 Hz, 1H, ArH), 6.36 (d, $^3J_{HH}$ = 7.6 Hz, 1H, ArH), 6.21 (d, $^3J_{HH}$ = 7.3 Hz, 1H, ArH), 3.11 (s, 3H, NCH$_3$), 2.54 (s, 3H, ArCH$_3$) ppm. ^{31}P NMR (81 MHz, CDCl$_3$): δ −144.2 (sept, $^1J_{PF}$ = 713 Hz, PF$_6$) ppm. ^{19}F NMR (188 MHz, CDCl$_3$): δ −72.7 (d, $^1J_{PF}$ = 712 Hz, PF$_6$) ppm. HRMS (ESI-TOF) m/z (%): calcd. 674.1898; found 674.1923 (100) [(M − PF$_6$)$^+$].

[Ir(diFppy)$_2$(L3)]PF$_6$ (3b). A solution of L3 (63 mg, 0.21 mmol, 2.1 equiv), silver(I) oxide (28 mg, 0.12 mmol, 1.2 equiv), and [Ir(diFppy)$_2$(μ-Cl)]$_2$ (122 mg, 0.10 mmol, 0.5 equiv) in 12 mL of 1,2-dichloroethane was heated to reflux (95 °C) overnight. After cooling to ambient temperature, the mixture was filtered through Celite to remove silver residues. The Celite was washed with CH$_2$Cl$_2$, and the solvent was removed in vacuo. The residue was dissolved in 20 mL of CH$_2$Cl$_2$ and extracted three times with an aqueous KPF$_6$ solution (55 mg of KPF$_6$ in 40 mL of water per cycle). The combined organic layers were washed with water, dried over MgSO$_4$, and concentrated in vacuo. The crude product was purified by column chromatography on silica gel with CH$_2$Cl$_2$ and then CH$_2$Cl$_2$/acetone (4:1 v/v) as solvent. After evaporation of the solvent, the pure product obtained was a yellow solid. Yield: 91 mg (0.10 mmol, 50%). ^{1}H NMR (400 MHz, acetone-d_6): δ 8.41−8.36 (m, 3H, ArH), 8.28 (br d, $^3J_{HH}$ = 5.8 Hz, 1H, ArH), 8.20 (br s, 1H, ArH), 8.05 (t, $^3J_{HH}$ = 7.8 Hz, 2H, ArH), 7.91 (br d, $^3J_{HH}$ = 5.8 Hz, 1H, ArH), 7.75 (d, $^3J_{HH}$ = 5.8 Hz, 1H, ArH), 7.52 (d, $^4J_{HH}$ = 2.2 Hz, 1H, ArH), 7.33 (br d, $^3J_{HH}$ = 5.8 Hz, 1H, ArH), 7.25−7.21 (m, 2H, ArH), 6.75−6.64 (m, 2H, ArH), 5.91 (dd, $^3J_{HH}$ = 8.9 Hz, $^4J_{HH}$ = 2.3 Hz, 1H, ArH), 5.73 (dd, $^3J_{HH}$ = 8.0 Hz, $^4J_{HH}$ = 2.4 Hz, 1H, ArH), 3.39 (s, 3H, NCH$_3$), 2.58 (s, 3H, ArCH$_3$) ppm. ^{31}P NMR (81 MHz, acetone-d_6): δ −144.2 (sept, $^1J_{PF}$ = 707 Hz, PF$_6$) ppm. ^{19}F NMR (188 MHz, acetone-d_6): δ −72.5 (d, $^1J_{PF}$ = 707 Hz, PF$_6$), −108.0 (vq, J = 9.1 Hz, ArF), −108.5 (vq, J = 9.5 Hz, ArF), −109.9 (vt, J = 11.4 Hz, ArF), −110.5 (vt, J = 11.5 Hz, ArF) ppm. HRMS (ESI-TOF) m/z (%): calcd. 746.1520; found 746.1531 (100) [(M − PF$_6$)$^+$].

[Ir(ppy)$_2$(L4)]PF$_6$ (4a). A solution of L4 (60 mg, 0.21 mmol, 2.1 equiv), silver(I) oxide (28 mg, 0.12 mmol, 1.2 equiv), and [Ir(ppy)$_2$(μ-Cl)]$_2$ (107 mg, 0.10 mmol, 0.5 equiv) in 12 mL of 1,2-dichloroethane was heated to reflux (95 °C) overnight. After cooling to ambient temperature, the mixture was filtered through Celite to remove silver residues. The Celite was washed with CH$_2$Cl$_2$, and the solvent was removed in vacuo. The residue was dissolved in 20 mL of CH$_2$Cl$_2$ and

extracted three times with an aqueous KPF$_6$ solution (55 mg of KPF$_6$ in 40 mL of water per cycle). The combined organic layers were washed with water, dried over MgSO$_4$, and concentrated in vacuo. The crude product was purified by column chromatography on silica gel with CH$_2$Cl$_2$ and then CH$_2$Cl$_2$/acetone (4:1 v/v) as solvent. After evaporation of the solvent, the pure product obtained was a yellow solid. Yield: 79 mg (0.098 mmol, 49%). ^{1}H NMR (400 MHz, acetone-d_6): δ 8.39 (d, $^4J_{HH}$ = 2.2 Hz, 1H, ArH), 8.31−8.21 (m, 5H, ArH), 8.00−7.95 (m, 2H, ArH), 7.92−7.85 (m, 4H, ArH), 7.50−7.46 (m, 2H, ArH), 7.19−7.14 (m, 2H, ArH), 7.07 (td, $^3J_{HH}$ = 7.5 Hz, $^4J_{HH}$ = 1.3 Hz, 1H, ArH), 7.01−6.96 (m, 2H, ArH), 6.87 (td, $^3J_{HH}$ = 7.4 Hz, $^4J_{HH}$ = 1.4 Hz, 1H, ArH), 6.48 (d, $^3J_{HH}$ = 7.6 Hz, 1H, ArH), 6.32 (d, $^3J_{HH}$ = 7.4 Hz, 1H, ArH), 3.31 (s, 3H, NCH$_3$) ppm. ^{31}P NMR (81 MHz, acetone-d_6): δ −144.3 (sept, $^1J_{PF}$ = 707 Hz, PF$_6$) ppm. ^{19}F NMR (188 MHz, acetone-d_6): δ −72.7 (d, $^1J_{PF}$ = 706 Hz, PF$_6$) ppm. HRMS (ESI-TOF) m/z (%): calcd. 660.1741; found 660.1736 (100) [(M − PF$_6$)$^+$].

[Ir(diFppy)$_2$(L4)]PF$_6$ (4b). A solution of L4 (60 mg, 0.21 mmol, 2.1 equiv), silver(I) oxide (28 mg, 0.12 mmol, 1.2 equiv), and [Ir(diFppy)$_2$(μ-Cl)]$_2$ (122 mg, 0.10 mmol, 0.5 equiv) in 12 mL of 1,2-dichloroethane was heated to reflux (95 °C) overnight. After cooling to ambient temperature, the mixture was filtered through Celite to remove silver residues. The Celite was washed with CH$_2$Cl$_2$, and the solvent was removed in vacuo. The residue was dissolved in 20 mL of CH$_2$Cl$_2$ and extracted three times with an aqueous KPF$_6$ solution (55 mg of KPF$_6$ in 40 mL of water per cycle). The combined organic layers were washed with water, dried over MgSO$_4$, and concentrated in vacuo. The crude product was purified by column chromatography on silica gel with CH$_2$Cl$_2$ and then CH$_2$Cl$_2$/EtOAc (9:1 v/v) as solvent. After evaporation of the solvent, the pure product obtained was a yellow solid. Yield: 119 mg (0.136 mmol, 68%). ^{1}H NMR (400 MHz, acetone-d_6): δ 8.45−8.30 (m, 6H, ArH), 8.08 (br t, $^3J_{HH}$ = 7.0 Hz, 2H, ArH), 7.98 (br d, $^3J_{HH}$ = 5.2 Hz, 1H, ArH), 7.93 (br d, $^3J_{HH}$ = 6.0 Hz, 1H, ArH), 7.58 (d, $^4J_{HH}$ = 2.2 Hz, 1H, ArH), 7.56−7.52 (m, 1H, ArH), 7.28−7.23 (m, 2H, ArH), 6.79−6.68 (m, 2H, ArH), 5.93 (dd, $^3J_{HH}$ = 9.0 Hz, $^4J_{HH}$ = 2.3 Hz, 1H, ArH), 5.76 (dd, $^3J_{HH}$ = 7.9 Hz, $^4J_{HH}$ = 2.3 Hz, 1H, ArH), 3.44 (s, 3H, NCH$_3$) ppm. ^{31}P NMR (81 MHz, acetone-d_6): δ −144.2 (sept, $^1J_{PF}$ = 707 Hz, PF$_6$) ppm. ^{19}F NMR (188 MHz, acetone-d_6): δ −72.3 (d, $^1J_{PF}$ = 706 Hz, PF$_6$), −108.0 (vq, J = 9.2 Hz, ArF), −108.4 (vq, J = 9.6 Hz, ArF), −109.8 (vt, J = 11.6 Hz, ArF), −110.5 (vt, J = 11.6 Hz, ArF) ppm. HRMS (ESI-TOF) m/z (%): calcd. 732.1364; found 732.1371 (100) [(M − PF$_6$)$^+$].

[Ir(ppy)$_2$(L5)]PF$_6$ (5a). A solution of L5 (91 mg, 0.21 mmol, 2.1 equiv), silver(I) oxide (48 mg, 0.21 mmol, 2.1 equiv), and [Ir(ppy)$_2$(μ-Cl)]$_2$ (107 mg, 0.10 mmol, 0.5 equiv) in 12 mL of 1,2-dichloroethane was heated to reflux (95 °C) overnight. After cooling to ambient temperature, the mixture was filtered through Celite to remove silver residues. The Celite was washed with CH$_2$Cl$_2$, and the solvent was removed in vacuo. The residue was dissolved in 20 mL of CH$_2$Cl$_2$ and extracted three times with an aqueous KPF$_6$ solution (55 mg of KPF$_6$ in 40 mL of water per cycle). The combined organic layers were washed with water, dried over MgSO$_4$, and concentrated in vacuo. The crude product was purified by column chromatography on silica gel with CH$_2$Cl$_2$ and then CH$_2$Cl$_2$/acetone (4:1 v/v) as solvent. After evaporation of the solvent, the pure product obtained was a yellow solid. Yield: 70 mg (0.085 mmol, 43%). ^{1}H NMR (400 MHz, CDCl$_3$): δ 8.21 (d, $^3J_{HH}$ = 5.9 Hz, 2H, NCH), 7.94 (d, $^3J_{HH}$ = 8.2 Hz, 2H, NCH), 7.85−7.80 (m, 2H, ArH), 7.64 (d, $^3J_{HH}$ = 7.8 Hz, 2H, ArH), 7.51 (br, 2H, ArH), 7.07 (td, $^3J_{HH}$ = 6.0 Hz, $^4J_{HH}$ = 1.0 Hz, 2H, ArH), 6.94−6.90 (m, 2H, ArH), 6.80 (td, $^3J_{HH}$ = 7.4 Hz, $^4J_{HH}$ = 1.1 Hz, 2H, ArH), 6.76 (t, $^4J_{HH}$ = 1.8 Hz, 2H, ArH), 6.36 (d, $^3J_{HH}$ = 7.5 Hz, 2H, ArH), 6.18 (s, 2H, NCH$_2$N), 2.84 (s, 6H, NCH$_3$) ppm. ^{31}P NMR (81 MHz, CDCl$_3$): δ −144.2 (sept, $^1J_{PF}$ = 712 Hz, PF$_6$) ppm. ^{19}F NMR (188 MHz, CDCl$_3$): δ −72.4 (d, $^1J_{PF}$ = 712 Hz, PF$_6$) ppm. HRMS (ESI-TOF) m/z (%): calcd. 677.2006; found 677.1983 (100) [(M − PF$_6$)$^+$].

Scheme 1. General Synthetic Scheme for Charged Iridium(III) Complexes 1−5

R = H (**1-5a**)
R = F (**1-5b**)
Y = C or N

LH⁺,X⁻ =   **L1**   **L2**   **L3**   **L4**   **L5**
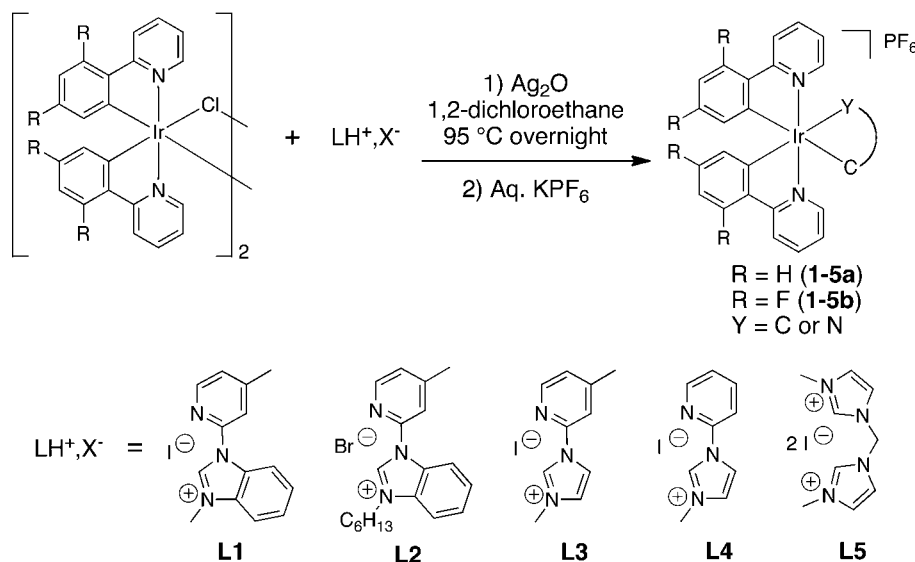
RESULTS AND DISCUSSION

Synthesis and X-ray Crystal Structures. As depicted in Scheme 1, the complexes were synthesized according to previously reported methods.[25] The N^C: ligands **L1** to **L4** were obtained by copper-catalyzed C−N couplings of 2-bromopyridine derivatives and imidazole or benzimidazole, respectively, followed by alkylation with alkyl halides. As previously reported, addition of Ag₂O to the ligands generated in situ the corresponding silver carbene complexes, which were reacted directly with the chloro-bridged iridium dimers to transfer the carbene ligands to the iridium center. An additional role of the silver cation was to promote the removal of the chloride anion from the iridium center. After reaction, the complexes **1−5a,b** were purified by column chromatography on silica gel and isolated as PF₆ salts.

Single crystals suitable for X-ray diffraction analysis were grown by slow diffusion of heptane into a dichloromethane solution of the complexes. We report here the results for **2a**, **2b**, **3b**, **4b**, **5a**, and **5b**, whereas the X-ray crystal structures of **1a**, **1b**,[25] **4a**, **4b**,[26] and **5b**[11] were reported previously. The perspective view of **3b** is shown in Figure 1, and other complexes are shown in the Supporting Information, Figure S1 along with the crystallographic data in Table S1. Selected bond distances and angles for all structures are given in Table 1. We found here only minor differences in the structure of **5b**, which are attributed to the different cocrystallized solvent (acetonitrile in the previous report, dichloromethane in the present one). All the complexes have a slightly distorted octahedral geometry around the iridium center. In all cases the pyridine groups of the C^N ligands are in trans position to each other. There are only minor differences between the complexes with pyridine−imidazole ancillary ligands. Note that the Ir−C₂ bond (C₂ is the coordinated carbon trans to the pyridine of the ancillary ligand) is always shorter than the Ir−C₃ bond (C₃ is the coordinated carbon trans to the carbene of the ancillary ligand). This reflects the stronger trans effect of the carbene compared to the pyridine. The N^C: ancillary ligands are almost flat, while the :C^C: ligands are significantly distorted because of the methylene bridge. As a consequence, the bite angle is about 9° wider for the :C^C: ligands than for the N^C: ligands.
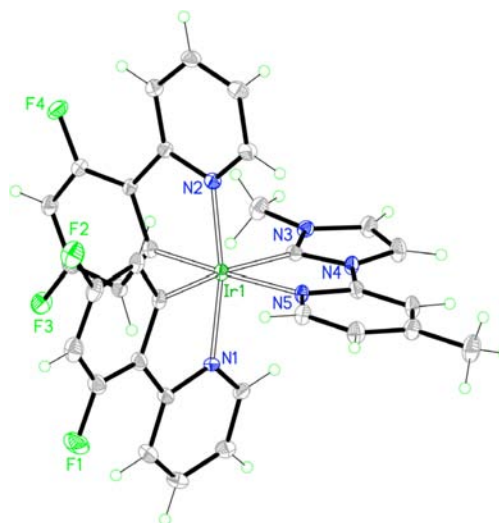

Figure 1. Perspective view of the cation of **3b**.

Electrochemistry. The electrochemical data for the complexes **1−5a,b** were measured versus the Fc⁺/Fc couple in acetonitrile with TBAPF₆ as the electrolyte. The results are reported in Table 2 together with the energies calculated for the HOMO and LUMO. As expected, the attachment of fluorine atoms to the phenyl rings produces a large anodic shift (∼0.3 eV), well paralleled by the HOMO stabilization obtained with the theoretical calculations (∼0.27 V), because the HOMO largely resides on the phenyl rings of the ppy ligands (see below). A smaller positive shift (∼0.1 V) is also measured for the reduction potentials in passing from **1−5a** to **1−5b**, indicating that the fluorine substituents also influence the energy of the LUMO because this orbital is also located on the ppy ligands, with some contribution from the phenyl rings. Overall, there are only minor differences throughout the series of N^C: ancillary ligands. This is particularly true for the diFppy series, in which the oxidation potentials are found between 1.19 and 1.22 V versus Fc⁺/Fc. Note that the replacement of the methyl group in **L1** with the longer n-hexyl chain in **L2** slightly enhances the oxidation potential (see **1a** vs **2a** and **1b** vs **2b**), an effect similarly observed for the complexes

Table 1. Selected Bond Distances (Å) and Angles (°) for Complexes 2a, 2b, 3b, 4b, 5a, and 5b

	2a	2b	3b	4b	5a	5b
			Distances			
Ir−N$_1$(C)	2.150(3)	2.1607(18)	2.164(3)	2.170(4)	2.127(3)	2.125(6)
Ir−C$_1$	2.066(4)	2.072(2)	2.076(4)	2.060(5)	2.106(3)	2.095(5)
Ir−N$_2$	2.062(3)	2.053(2)	2.045(3)	2.056(4)	2.055(2)	2.057(4)
Ir−N$_3$	2.063(3)	2.062(2)	2.064(3)	2.061(4)	2.065(2)	2.078(4)
Ir−C$_2$	2.025(4)	2.020(2)	2.018(4)	2.019(5)	2.060(3)	2.063(6)
Ir−C$_3$	2.066(4)	2.056(2)	2.055(4)	2.045(5)	2.069(3)	2.062(5)
			Angles			
N$_1$(C)−Ir−C$_1$	76.28(14)	76.22(8)	76.49(14)	76.96(18)	84.03(10)	85.8(2)
C$_3$−Ir−C$_1$	172.13(15)	169.93(8)	170.68(15)	171.5(2)	175.33(10)	172.5(2)
C$_2$−Ir−N$_1$(C)	176.64(14)	177.80(8)	176.17(13)	176.43(18)	176.75(11)	171.2(2)
N$_3$−Ir−N$_2$	170.63(12)	168.56(7)	168.86(13)	170.40(17)	168.11(9)	171.31(18)
C$_2$−Ir−C$_3$	84.62(16)	88.48(8)	89.13(15)	88.31(19)	84.81(10)	83.5(2)
C$_3$−Ir−N$_1$(C)	95.92(14)	93.72(8)	94.61(14)	94.68(18)	92.50(10)	92.0(2)
C$_2$−Ir−C$_1$	103.23(16)	101.57(8)	99.82(15)	100.1(2)	98.75(10)	99.5(2)

Table 2. Experimental Electrochemical Potentials and HOMO and LUMO Energies, Calculated at the B3LYP/(6-31G**/LANL2DZ) Level, of Complexes 1−5a,b

complex	E_{ox} (V)[a]	E_{red} (V)[a]	E_{HOMO} (eV)	E_{LUMO} (eV)	complex	E_{ox} (V)[a]	E_{red} (V)[a]	E_{HOMO} (eV)	E_{LUMO} (eV)
1a	0.86	−2.43	−5.50	−1.54	**1b**	1.19	−2.26	−5.77	−1.61
		−2.76					−2.54		
2a	0.91	−2.39	−5.50	−1.54	**2b**	1.21	−2.30	−5.77	−1.61
		−2.70					−2.58		
3a	0.84	−2.43	−5.44	−1.53	**3b**	1.19	−2.33	−5.72	−1.60
		−2.73					−2.61		
4a	0.86	−2.34	−5.45	−1.54	**4b**	1.22	−2.27	−5.73	−1.61
		−2.67					−2.59		
5a	0.81	−2.54	−5.42	−1.45	**5b**	1.10	−2.41	−5.66	−1.53
		−2.83					−2.71		

[a]From CV measurements, $E = 1/2(E_{pa} + E_{pc})$; 0.1 M acetonitrile/TBAPF$_6$ vs Fc$^+$/Fc.

with a :C^C: ancillary ligand.[11] Replacement of the benzimidazole for an imidazole unit in the ancillary ligand has apparently no impact on the redox potentials (**1a** vs **3a**). On the other hand, changing the N^C: for the :C^C: ligand (**5a** and **5b**) leads to a destabilization of both the oxidation and the reduction potential due to the stronger donor character of the carbene moiety compared to the pyridine group.

Photophysical Properties. All the complexes (**1−5a,b**) are stable in both CH$_3$CN and CH$_2$Cl$_2$ solutions over months and do not display any degradation under standard experimental conditions, including irradiation. The ultraviolet−visible (UV−vis) absorption spectra of complexes **1−5a** recorded in CH$_2$Cl$_2$ solution at room temperature are displayed in Figure 2. The strong absorption bands in the spectral region below 300 nm exhibit molar absorption coefficients (ε) between (2.0 and 5.5) × 10^4 M^{-1} cm^{-1}, which originate from the spin-allowed $^1\pi-\pi^*$ electronic LC transitions. The more intense ε values found for **1a** and **2a** are due to the extended benzimidazole aromatic moieties on the carbene subunits of the ancillary ligands. The structureless
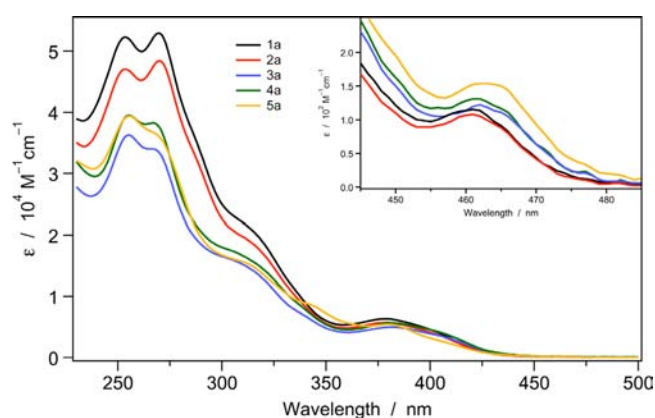

Figure 2. Absorption spectra of **1−5a** in CH$_2$Cl$_2$ at 298 K. The T$_1$ absorption transitions are magnified in the inset.

bands at 300−360 nm can be assigned both to phenyl-to-pyridine $\pi-\pi^*$ ligand-to-ligand (interligand) charge transfer (LLCT) transitions and to Ir(d$_\pi$)-to-phenylpyridine MLCT

transitions with a predominant singlet spin multiplicity.[11] The lower-lying bands in the visible region (>360 nm) can be attributed to both singlet and triplet MLCT transitions, which, however, have a strong $\pi-\pi^*$ character.[44]

The very weak, lowest-energy absorption bands (around 463 nm, $\varepsilon \approx 100-150$ M^{-1} cm^{-1}) that are magnified in the inset of Figure 2 can be identified as the spin-forbidden electronic transition from the ground state directly to the triplet emitting state (T$_1$).[14] The small spectral shift between the T$_1$ absorption and emission bands (412 cm^{-1}) suggests that the emitting state has a weak MLCT character and a pronounced $\pi-\pi^*$ LC contribution (see below). To further support this hypothesis, the absorption spectra were also recorded in more polar acetonitrile (see Figure S2 in the Supporting Information) and showed no substantial spectral shift.

The absorption spectra of the fluorinated series (**1**−**5b**) recorded in CH$_2$Cl$_2$ solution at room temperature are displayed in the Supporting Information, Figure S3. Remarkable differences compared to the **1**−**5a** series are observed mainly in the visible region at wavelength >350 nm. In fact, in this case, the singlet and triplet MLCT transitions display a blue shift of around 20 nm (975 cm^{-1}), and the lowest-energy absorption bands associated with the T$_1$ state are found at 443 nm ($\varepsilon \approx$ 100−200 M^{-1} cm^{-1}). A large hypsochromic shift upon replacing unsubstituted C^N phenylpyridines with difluorinated ones is a common finding for both neutral[14,45] and cationic[8,46−48] iridium(III) complexes. In fact, the attachment of electron-withdrawing substituents to the C^N ligands results in a significant stabilization of the HOMO (Table 2), which is located partially on the iridium metal and on the phenyl moieties of the phenylpyridines (see below).

The room temperature luminescence spectra of **1**−**5a** are reported in Figure 3. All the complexes display a strongly
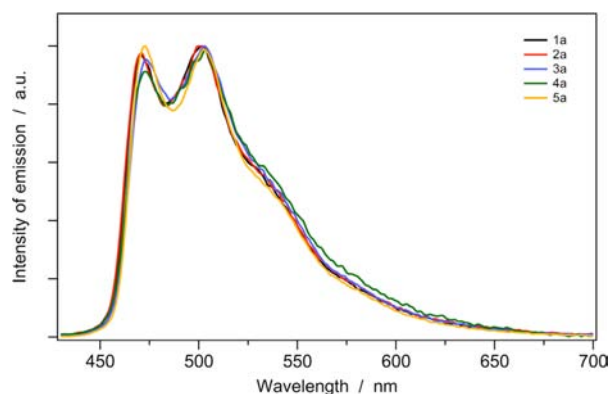

Figure 3. Normalized emission spectra of **1**−**5a** in CH$_2$Cl$_2$ at room temperature (λ_{exc} = 360 nm).

structured band, indicating that the emissive excited states have a pronounced LC $\pi-\pi^*$ character with a weaker MLCT contribution. No spectral shift is observed upon increasing the polarity of the solvent (see the data in acetonitrile, Supporting Information, Figure S4). Upon cooling of the solutions to 77 K, the emission spectra of the complexes exhibit a slight blue shift (~5 nm; ~200 cm^{-1}) and narrower, more highly resolved vibronic progressions (see Figure 4). The lack both of solvatochromism and of a relevant rigidochromic shift further suggests the predominant LC $\pi-\pi^*$ character of the emitting triplet state. These considerations are essentially the same also
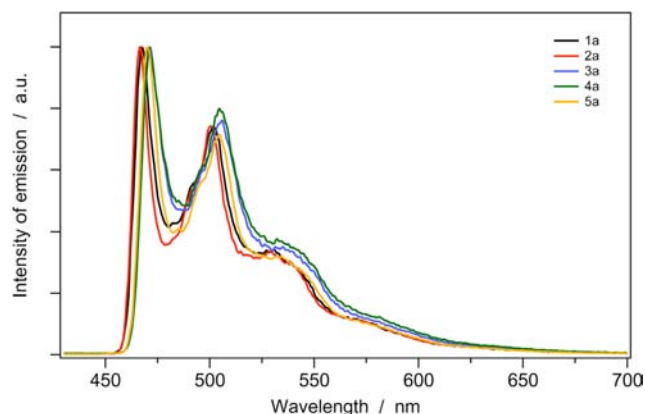

Figure 4. Normalized emission spectra of **1**−**5a** in CH$_2$Cl$_2$ at 77 K (λ_{exc} = 360 nm).

for the fluorinated complexes **1**−**5b** (Supporting Information, Figures S5−S7).

All the complexes having N^C: ligands (**1**−**4a,b**) show almost identical photophysical properties (Tables 3 and 4), demonstrating that chemical modifications on this type of ancillary ligand do not affect the nature of the excited state. In fact, as confirmed by theoretical calculations (see below), the frontier electronic levels of these complexes primarily involve the π-orbitals of the C^N ligands. Furthermore, the substituents of ligands **L1**−**4** are too far apart from the iridium(III) center to significantly alter the ligand field strength around the metal core. A minor red shift of 2−3 nm (~100 cm^{-1}) is observed in the case of the :C^C: complexes (**5a,b**), if compared to the N^C: analogues (**1**−**4a,b**). Because of the lack of a strong contribution from the ancillary ligand to the HOMO−LUMO transition, such a bathochromic shift is ascribed to a slight difference in the ligand field strength.

In room temperature solution, the N^C: complexes (**1**−**4a,b**) show very low Φ_{PL}, almost 2 orders of magnitude lower than those for the :C^C: analogues (**5a** and **5b**) (~0.5% vs ~30% in CH$_2$Cl$_2$). From the Φ_{PL} and the τ values, assuming a unitary intersystem crossing efficiency, the radiative and the overall nonradiative rate constants (k_r and k_{nr}, respectively) were calculated and are summarized in Table 3. In spite of almost comparable k_r values (~1.5 × 10^5 s^{-1}), the N^C: complexes display k_{nr} values around 80 times higher than those for the :C^C: analogues. These findings strongly suggest that (i) both families have T$_1$ excited states very similar in nature, and (ii) in the case of the N^C: complexes (at least in room temperature solution), nonradiative deactivation pathways involving thermally accessible upper-lying states play a fundamental role in deactivating the T$_1$ excited states.[44] In fact, at 77 K all the complexes (**1**−**5a,b**) show very strong phosphorescence, and both families exhibit almost identical excited-state lifetimes (~4 μs for complexes **1**−**5a**). A very similar behavior is observed in PMMA thin films (Table 4 and Supporting Information, Figures S8 and S9), where all the complexes display absolute emission quantum yields higher than 23% and lifetimes around 3 μs. These experimental findings can be rationalized in accord with the results of the theoretical study (vide infra). In fact, the DFT calculations predict that, except for complexes **5a,b**, there are low-energy nonradiative metal-centered (MC) states close to the emitting T$_1$ level. Such MC states are highly distorted, and, upon full geometrical relaxation occurring in RT solution, they may

Table 3. Photophysical Data of Complexes 1−5a,b at Room Temperature in CH$_2$Cl$_2$ and in CH$_3$CN

	CH$_2$Cl$_2$ at 298 K					CH$_3$CN at 298 K				
complex	λ_{em} (nm)	Φ_{PL} (%)	τ (ns)	k_r (10^5 s^{-1})	k_{nr} (10^7 s^{-1})	λ_{em} (nm)	Φ_{PL} (%)	τ (ns)	k_r (10^5 s^{-1})	k_{nr} (10^7 s^{-1})
1a	471, 502	0.6	37	1.62	2.69	471, 500	1.0	70	1.43	1.41
2a	471, 502	0.5	35	1.43	2.84	472, 500	1.1	71	1.55	1.39
3a	473, 503	0.8	46	1.74	2.16	475, 501	1.4	75	1.87	1.31
4a	472, 503	0.3	19	1.58	5.25	474, 502	0.6	36	1.67	2.76
5a	472, 502	28.5	1870	1.52	0.04	475, 503	37.5	2280	1.64	0.03
1b	451, 480	1.3	154	0.84	0.64	451, 480	2.4	295	0.81	0.33
2b	451, 480	1.6	140	1.14	0.70	451, 480	3.1	282	1.10	0.34
3b	451, 480	1.2	92	1.30	1.07	452, 481	1.9	115	1.65	0.85
4b	451, 480	0.7	47	1.49	2.11	451, 480	1.0	68	1.47	1.46
5b	454, 482	36.2	3130	1.16	0.02	456, 483	24.0	1910	1.26	0.04

Table 4. Photophysical Data of Complexes 1−5a,b at 77 K in CH$_3$CN and in Solid State

	CH$_3$CN glass at 77 K		neat film at 298 K		PMMA 1% w/w at 298 K		
complex	λ_{em} (nm)	τ (μs)	λ_{em} (nm)^a	Φ_{PL} (%)	λ_{em} (nm)	Φ_{PL} (%)	τ (μs)
1a	472, 501	4.3	509	1.6	472, 501	38.9	3.2
2a	471, 502	4.5	481^{sh}, 505	2.4	473, 501	42.6	3.3
3a	473, 503	4.1	488^{sh}, 507	2.4	476, 503	32.4	2.5
4a	472, 503	4.1	507	2.5	474, 502	23.7	2.4
5a	472, 501	4.3	507	1.7	474, 504	50.2	2.7
1b	446, 478, 513	4.9	510	2.3	450, 480	33.6	3.4
2b	447, 480, 506	6.6	457, 484	4.7	452, 480	43.8	3.8
3b	448, 480, 507	5.4	463, 490	3.0	452, 480	35.5	3.0
4b	448, 480, 510	6.0	462^{sh}, 485	1.8	452, 480	25.9	3.1
5b	446, 478, 513	4.9	462^{sh}, 485	3.5	454, 481	58.2	3.2

^{a}sh denotes a shoulder.

become the lowest triplet. Instead, in frozen solvent and at room temperature in solid matrix the population or the full relaxation of these MC states, or both, are prevented, so that T_1 remains the lowest-emitting triplet, as in the case of the :C^C: complexes. This picture can explain both the low Φ_{PL} of 1−4a,b in room temperature solution and also the considerable enhancement of Φ_{PL} observed in the solid state.

On the other hand, in neat films triplet−triplet annihilation processes start to play an important role; consequently, Φ_{PL} are dramatically reduced (Table 4), and τ are no longer monoexponential. For most of these complexes, a red shift of the emission occurs in going from solution to neat solid as a result of the band broadening and of the change of the relative intensities of the luminescence peaks (Figure 5, Table 4, and Supporting Information, Figure S10). Although bulky spectator groups are often attached to chelating ligands to reduce aggregation of the metal complex, which causes red-shift and emission quenching in neat solids,[3] the long *n*-hexyl chain anchored to the ancillary ligands of complexes 2a,b is not sufficient to prevent the quenching effect in the film.

Theoretical Calculations. To gain further insight into the photophysical properties, the molecular and electronic structures of the cations of complexes 1−5a,b, in both ground and excited states, were investigated by performing DFT calculations at the B3LYP/(6-31G**/LANL2DZ) level in the presence of the solvent (acetonitrile). The main interests were (i) to gain support for the emission originating from the C^N ligands, in contrast to the charged iridium complexes having bidentate N^N chelators where emission strongly involves such ancillary ligands, and (ii) to rationalize the higher Φ_{PL} measured for complexes 5a and 5b bearing :C^C: ancillary
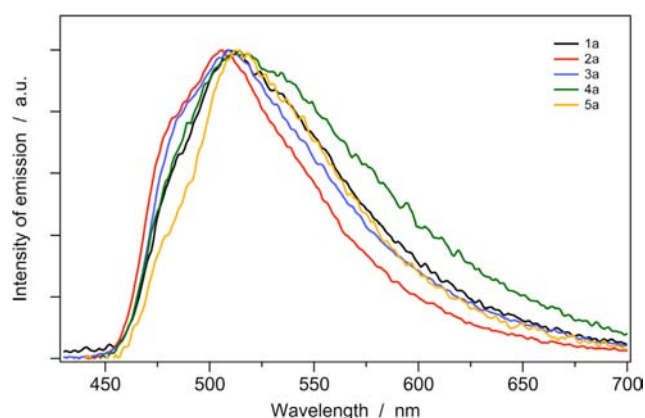

Figure 5. Room temperature normalized emission spectra of 1−5a as neat films (λ_{exc} = 360 nm).

ligands. DFT calculations were recently reported for 4a and 4b, but they were performed in the absence of solvent effects.

Ground State. Calculations in the electronic ground state (S$_0$) correctly reproduce the near-octahedral coordination of the Ir metal observed in the X-ray structures and predict geometric parameters in good accord with the experimental data. Table 5 collects the optimized values calculated for the bond distances and the bond angles defining the coordination sphere of the iridium center in complexes 3b and 5b taken as representative examples of complexes bearing N^C: and :C^C: ancillary ligands, respectively (Table S2 in the Supporting Information gathers the geometrical parameters computed for all the complexes). The structural trends inferred from the X-ray data are well supported by the theoretical calculations. For

Table 5. Selected Bond Distances (in Å) and Angles (°) Calculated for Complexes 3b and 5b in the Singlet Ground State (S_0) and in the T_1 and the Triplet Metal-Centered (^{3}MC) Excited States[a]

	3b				5b		
	exp	S_0	T_1	^{3}MC[b]	exp	S_0	T_1
			Distances				
Ir−N$_1$(C)	2.164(3)	2.231	2.251		2.125(6)	2.172	2.179
Ir−C$_1$	2.076(4)	2.107	2.120	2.150	2.095(5)	2.160	2.170
Ir−N$_2$	2.045(3)	2.081	2.092	2.077	2.057(4)	2.091	2.102
Ir−N$_3$	2.064(3)	2.091	2.059	2.086	2.078(4)	2.099	2.066
Ir−C$_2$	2.018(4)	2.018	2.014	2.056	2.063(6)	2.061	2.060
Ir−C$_3$	2.055(4)	2.064	2.039	2.054	2.062(5)	2.068	2.046
			Angles				
N$_1$(C)−Ir−C$_1$	76.49(14)	75.34	74.87		85.8(2)	84.37	84.49
C$_3$−Ir−C$_1$	170.68(15)	169.76	168.64	127.66	172.5(2)	174.56	174.42
C$_2$−Ir−N$_1$(C)	176.17(13)	175.12	175.11		171.2(2)	175.16	176.00
N$_3$−Ir−N$_2$	168.86(13)	172.43	173.33	175.74	171.31(18)	170.57	171.46
C$_2$−Ir−C$_3$	89.13(15)	89.14	94.07	107.95	83.5(2)	85.63	86.47
C$_3$−Ir−N$_1$(C)	94.61(14)	95.07	90.26		92.0(2)	92.63	92.02
C$_2$−Ir−C$_1$	99.82(15)	100.61	100.90	124.36	99.5(2)	97.72	97.28

[a]X-ray values from Table 1 are included for comparison. [b]The values of the Ir−N$_1$ distance and of the angles where N$_1$ participates are not given for the ^{3}MC state because the pyridine ring of the ancillary ligand is decoordinated in this state.

instance, in complex **3b** the Ir−C$_2$ distance (2.018 Å) is predicted to be significantly shorter than that found for the Ir−C$_3$ distance (2.064 Å), showing the stronger trans effect of the carbene compared to the pyridine and in good agreement with the X-ray data (2.018(4) and 2.055(4) Å, respectively). For the :C^C: complex **5b**, the Ir−C$_2$ and Ir−C$_3$ bonds have a similar length (~2.065 Å), which is almost identical to that calculated for the Ir−C$_3$ bond in complex **3b** (2.064 Å). As observed in the X-ray structures, the N^C: ancillary ligands are predicted to be almost flat, whereas the carbene rings of the :C^C: ligand in complexes **5a** and **5b** are not in the same plane because of the methylene bridge. To maximize the interaction with the iridium core, the :C^C: ligand loses its planarity, and the imidazolium rings are twisted by an average angle of 52.3°. The larger bite angle computed for the :C^C: ligand (**5b**: 84.4°), when compared with the N^C: ligand (**3b**: 75.3°), agrees with the X-ray values (85.8 and 76.5°, respectively). The largest difference between computed and X-ray data corresponds to the coordinate Ir−N and Ir−C(carbene) bonds, whose distances are theoretically overestimated as is commonly observed when using the B3LYP functional.[25,49,50]

Figure 6 displays the energy and the atomic orbital composition calculated for the frontier molecular orbitals (MOs) of complex **3b** (see Table S4 in the Supporting Information for a detailed description of the orbitals of all the complexes). These MOs provide information about the nature of the excited states that mainly determine the absorption and emission properties. For all the complexes, the HOMO, LUMO, and LUMO+1 show the topology depicted in Figure 6 for **3b**. As expected, the HOMO is composed of a mixture of iridium d$_\pi$ orbitals and phenyl π orbitals distributed almost equally among the two C^N ppy ligands. The HOMO-1 to HOMO-4 also mainly involve the Ir center and the ppy ligands. The LUMO and LUMO+1 show almost no contribution from the metal, and, in contrast to what is usually found for charged iridium complexes bearing bidentate N^N ancillary ligands, for which the LUMO is located on the ancillary ligand, they mainly reside on the pyridine rings of the main C^N ligands and are separated by an energy difference of 0.09 eV because of the nonidentical geometries of the ligands. The main difference
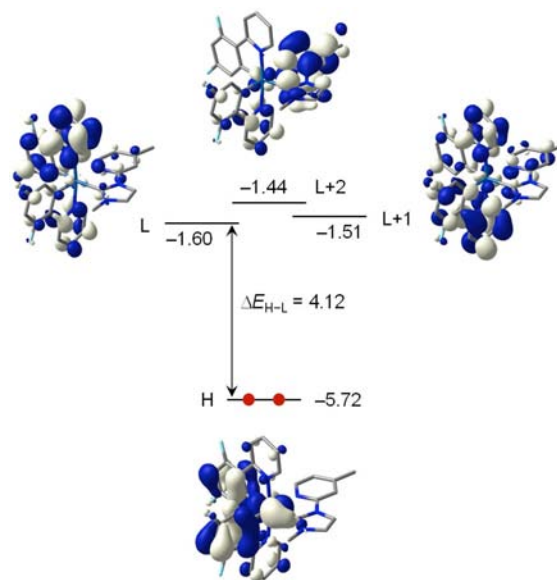

Figure 6. Energy diagram showing the electronic density contours (0.05 e bohr^{-3}) and the energy values (in eV) calculated for the frontier molecular orbitals of complex **3b**. H and L denote HOMO and LUMO, respectively.

between the electronic structure of complexes **1−4** bearing a N^C: ligand and complexes **5** is that for the former the LUMO+2, which is mainly located on the pyridine ring of the N^C: ligand, is close in energy to the LUMO and LUMO+1 (Figure 6). However, this is not the case for complexes **5** bearing a :C^C: ligand, for which the first empty molecular orbital involving the ancillary ligand appears as the LUMO+4 and lies very high in energy (1.40 eV) above the LUMO. The high energy of this orbital is due to the presence of two carbene units and to the methylene bridge that breaks the π conjugation between those units. As discussed in a subsequent section, these electronic differences play a relevant role in the nature of the lowest-energy triplet states and, thereby, in the photophysical properties of the complexes. Note that the HOMO−LUMO energy gap increases by ~0.20 eV in passing from the

Table 6. Lowest Triplet Excited States Calculated at the B3LYP/(6-31G**/LANL2DZ) Level for Complexes 3b and 5b[a]

complex	state	E (eV)	monoexcitations[b]	nature	description[c]
3b	T_1	2.93	H → L (36)	$\pi_{ppy} + d_\pi(Ir) \to \pi^*_{ppy}$	$^3LC/^3MLCT$
			H−2 → L (24)		
	T_2	2.96	H → L + 1 (33)	$\pi_{ppy} + d_\pi(Ir) \to \pi^*_{ppy}$	$^3LC/^3MLCT$
	T_3	3.37	H → L (39)	$\pi_{ppy} + d_\pi(Ir) \to \pi^*_{ppy}$	$^3LC/^3MLCT$
	T_4	3.38	H → L + 1 (45)	$\pi_{ppy} + d_\pi(Ir) \to \pi^*_{ppy}$	$^3LC/^3MLCT$
	T_5	3.41	H → L+2 (26)	$d_\pi(Ir) + \pi_{ppy} \to \pi^*_{carbene}$	$^3MLCT/^3LLCT$
			H−1 → L+2 (16)		
	T_6	3.55	H → L+2 (61)	$d_\pi(Ir) + \pi_{ppy} \to \pi^*_{carbene}$	$^3MLCT/^3LLCT$
5b	T_1	2.94	H → L (17)	$\pi_{ppy} + d_\pi(Ir) \to \pi^*_{ppy}$	$^3LC/^3MLCT$
			H → L+1 (26)		
			H−2 → L+1 (19)		
	T_2	2.94	H → L (15)	$\pi_{ppy} + d_\pi(Ir) \to \pi^*_{ppy}$	$^3LC/^3MLCT$
			H−1 → L (26)		
			H → L+1 (15)		
	T_3	3.35	H → L (45)	$\pi_{ppy} + d_\pi(Ir) \to \pi^*_{ppy}$	$^3LC/^3MLCT$
			H−1 → L (17)		
	T_4	3.40	H → L+1 (31)	$\pi_{ppy} + d_\pi(Ir) \to \pi^*_{ppy}$	$^3LC/^3MLCT$
			H−2 → L+1 (21)		
	T_5	3.58	H−3 → L+1 (39)	$\pi_{ppy} + d_\pi(Ir) \to \pi^*_{ppy}$	$^3LC/^3MLCT$
	T_6	3.60	H−4 → L+1 (28)	$\pi_{ppy} + d_\pi(Ir) \to \pi^*_{ppy}$	$^3LC/^3MLCT$

[a]Vertical excitation energies (E), dominant monoexcitations with contributions greater than 15% (within parentheses), nature of the electronic transition, and description of the excited state are summarized. [b]H and L denote HOMO and LUMO, respectively. [c]LC, MLCT, and LLCT denote ligand-centered, metal-to-ligand charge transfer, and ligand-to-ligand charge transfer, respectively.
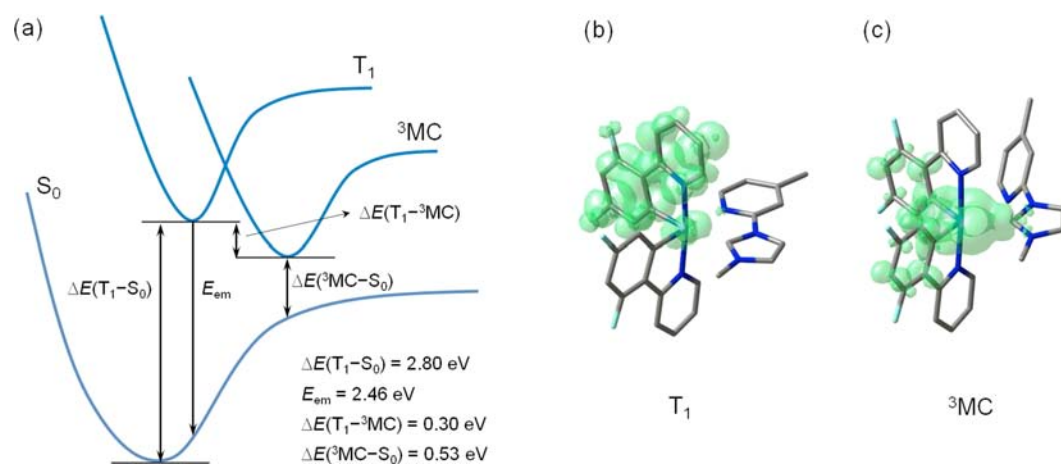

Figure 7. (a) Schematic energy diagram showing the adiabatic energy differences (ΔE) between the S_0, T_1, and ^3MC states and the emission energy (E_{em}) from T_1 calculated for **3b**. (b and c) Unpaired-electron spin-density contours (0.003 e bohr^{-3}) calculated for the fully relaxed T_1 and ^3MC states of **3b**, respectively.

nonfluorinated (∼3.95 eV) to the fluorinated (∼4.15 eV) complexes, in good correlation with the blue shift observed experimentally in both the absorption and the emission spectra.

Excited States. In light of the atomic orbital composition found for the HOMO and the LUMO/LUMO+1, the lowest-energy triplet states are expected to correspond to $\pi-\pi^*$ states mainly centered on the C^N ligands. To corroborate this suggestion and to investigate the nature of the emitting excited state, the low-lying triplet states of all the complexes were calculated at the optimized geometry of the ground state S_0 using the TD-DFT approach. The reliability of this approach was investigated by calculating the lowest-lying singlet state ($S_0 \to S_n$) transitions. The theoretical UV−vis spectra perfectly reproduce the spectral features observed in the experimental spectra (Figure S11 in the Supporting Information). Table 6

collects the vertical excitation energies and electronic descriptions computed for the six lowest-energy triplets of complexes **3b** and **5b** as representative examples.

The TD-DFT calculations predict that the two lowest-energy triplet states (T_1 and T_2) are almost degenerate and show a similar electronic nature for all the complexes. Both triplet states have a high multiconfigurational character, the largest contributions corresponding to the HOMO → LUMO and the HOMO → LUMO+1 monoexcitations (Table 6). The T_1 and T_2 states are therefore described as $\pi-\pi^*$ LC states involving the C^N ligands, where both the HOMO and the LUMO/LUMO+1 are mainly located (Figure 6), with a weak MLCT character due to the participation of the Ir atom in the HOMO. The only difference between T_1 and T_2 is the C^N ligand implied in the intraligand electronic transition. For complexes

1−4, the first excited states in which the ancillary ligand largely participates are the T_5 and T_6 triplet states that involve the electron monoexcitation to the LUMO+2 located on the N^C: ligand (see Table 6 and Figure 6 for complex **3b**). These states are computed to be 0.4−0.6 eV above the T_1/T_2 triplet states and show a mixed ^{3}MLCT/^{3}LLCT character. In the case of complexes **5a** and **5b**, the ^{3}MLCT/^{3}LLCT triplets are very high in energy because, as mentioned previously, the first virtual orbital involving the :C^C: ancillary ligand corresponds to the LUMO+4 and is calculated to be 1.4 eV above the LUMO. TD-DFT calculations therefore suggest that the emitting excited state for complexes **1−5** involves, in all cases, the C^N ligand and the Ir metal core, unlike what is found for complexes bearing N^N ancillary ligands with low-energy π^* orbitals.[3,12,24,49,51] This picture completely differs from that previously reported for **4a** and **4b** by Zhang et al., who performed TD-DFT calculations without taking into account the solvent and predited a ^{3}MLCT/^{3}LLCT character for the lowest-energy triplet.[26]

In addition to the TD-DFT study, the lowest triplet excited state T_1 was further examined by optimizing its geometry with the use of the spin-unrestricted UB3LYP approach. After full-geometry relaxation, the T_1 state is calculated to lie 2.67−2.69 eV above S_0 for complexes **1−5a** and 2.80−2.84 eV above S_0 for complexes **1−5b** (adiabatic energy differences, $\Delta E(T_1 − S_0)$ in Figure 7a). As depicted in Figure 7b for complex **3b**, the unpaired electrons in the T_1 state are mostly concentrated in one of the C^N ligands with a small contribution from the Ir atom (Ir, 0.166e; C^N ligand, 1.828e; N^C: ligand, 0.007e). A similar spin-density distribution is found for the T_2 state, which is located on the other C^N ligand, and for the rest of the complexes. The only difference between the nonfluorinated and the fluorinated series is that the spin density over the Ir metal core ranges from 0.233 to 0.308 e for complexes **1−5a** and decreases to 0.145−0.166 e for **1−5b** because of the absence or presence of the electron-withdrawing effect of the fluorines, respectively. Excitation to T_1 causes small changes (0.01−0.03 Å) in the coordination sphere of the complexes (Table 5). The theoretical calculations therefore confirm that the emitting state of complexes **1−5** has a ^{3}LC $\pi−\pi^*$ character with a weak ^{3}MLCT contribution, which mainly implies an electron promotion within the C^N ligands in good agreement with the experimental evidence. The large LC character of T_1 justifies the structured emission spectra observed experimentally at room temperature and the absence of a rigidochromic shift at low temperature (Figures 3 and 4).

To estimate the emission energy, the vertical energy difference between the emitting triplet and S_0 was determined by performing a single-point calculation of S_0 at the optimized minimum-energy geometry of T_1 (E_{em} in Figure 7a). Calculations led to vertical emission energies of 2.36−2.41 eV (525−515 nm) for complexes **1−5a** and of 2.46−2.52 eV (503−492 nm) for complexes **1−5b**. These values slightly underestimate the experimental energy of the second peak of the emission spectra, but correctly reproduce the blue shift of ~20 nm (975 cm^{-1}) observed in passing from the non-fluorinated to the fluorinated series (Table 3).

As previously performed for complexes incorporating N^C: ancillary ligands,[25] the presence of low-energy MC states was investigated at the UB3LYP level by starting from geometries optimized in the gas phase and then reoptimizing the geometries in the presence of the solvent. For complexes **1−4**, the calculations converged to the ^{3}MC state depicted in

Figure 7c for **3b**, in which the pyridine ring of the N^C: ligand is rotated around the inter-ring bond by 58.6° (the values calculated for the bond distances and the bond angles defining the coordination sphere of the iridium center are given in Table 5). The spin-density computed for this state confirms its MC nature since the Ir center accumulates a large part of the unpaired electrons (Figure 7c). The optimized geometry of the ^{3}MC state is similar for all complexes **1−4**, the major difference being the internal rotation angle of the N^C: ligand that has a value of 63−67° for complexes **1** and **2** with a benzimidazole ancillary ligand and of 54−58° for complexes **3** and **4** with an imidazole ancillary ligand. As can be seen in Figure 7c, the nitrogen atom of the pyridine ring is fully decoordinated in the ^{3}MC state, and the complex adopts a slightly distorted trigonal bipyramid molecular geometry. This is evidenced by the $C_3−Ir−C_1$ and $C_2−Ir−C_1$ bond angles that have values close to 125° in the ^{3}MC state (Table 5).

An important aspect is the relative energy position of the ^{3}MC state with respect to the emitting triplet state. After geometry relaxation, the ^{3}MC of complexes **1−4** is calculated to lie 0.3−0.4 eV (0.30 eV for **3b**) below the T_1 state (adiabatic energy differences, $\Delta E(T_1 − ^3MC)$ in Figure 7a). An effective population is therefore expected for the ^{3}MC, and this state would play a role in the deactivation of the emission process since, at its fully relaxed geometry, it lies close in energy to the S_0 state (~0.5 eV, $\Delta E(^3MC − S_0)$ in Figure 7a). This can explain the low Φ_{PL} experimentally observed for complexes **1−4** (Table 3).

In contrast to complexes **1−4**, the calculations were not able to localize the ^{3}MC state for the :C^C: complexes **5a,b**. The ^{3}MC state implies the decoordination of one of the carbene units and is expected at high energies because, as discussed previously, the empty orbitals implying the :C^C: ligand are found higher in energy than those for the N^C: ligands. The absence of the low-lying ^{3}MC explains the larger values observed for the Φ_{PL} of complexes **5a,b** (Table 3).

Temperature Dependence of τ. In order to understand the role played by thermally activated nonradiative decay processes on the luminescence properties, temperature-dependent experiments were carried out for complexes **4a** and **5a** as representative examples of the N^C: and the :C^C: families, respectively. One way to experimentally evaluate the relative energy position of the ^{3}MC states with respect to the emitting T_1 states in transition-metal complexes is to monitor the temperature dependence of the overall intrinsic deactivation rate constants, $k_{in}(T) = 1/\tau(T)$, where τ is the excited-state lifetime of a particular complex at a certain temperature T.[44,52,53] We chose to monitor the lifetimes of **4a** and **5a** between 77 and 350 K in butyronitrile solutions since this solvent forms a transparent glass at low temperature and also exhibits a relatively high boiling point.

In general, the changes of k_{in} over a wide temperature range entail several individual contributions to the decay process of the emitting T_1 state as the temperature increases, according to the equation $k_{in}(T) = k_0 + \sum_i k_i$. k_0 is a temperature-independent term and k_i is the rate constant of the ith step which contributes to the decay process. Previous works have shown that the k_i terms can be expressed as Arrhenius-type equations containing a frequency factor (A_i) and an activation energy barrier (ΔE_i): $k_i = A_i \exp(-\Delta E_i/k_B T)$.[52]

Figure 8 shows the evolution of k_{in} as a function of temperature, whereas Table 7 summarizes the values obtained
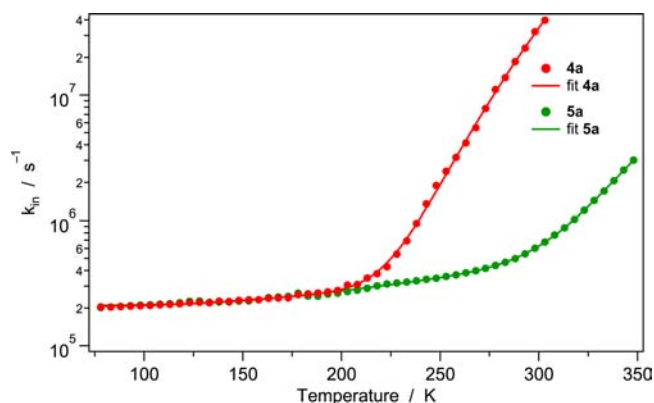
Figure 8. Temperature-dependent excited-state deactivation rates (k_{in} = $1/\tau$) of **4a** and **5a** as representative examples of the N^C: and the :C^C: families, respectively. The lines connecting the experimental points were fitted using eq 1 with two Arrhenius terms; the parameters are reported in Table 7. Excited-state lifetimes were determined from the luminescence decays with the time-correlated single photon counting technique.

for the k_0, A_i, and ΔE_i parameters from the nonlinear iterative fitting of k_{in} data as a function of temperature using the aforementioned equations with two Arrhenius terms:

$$k_{in}(T) = k_0 + A_1 \exp(-\Delta E_1/k_B T) + A_2 \exp(-\Delta E_2/k_B T) \tag{1}$$

The first term in eq 1 is the temperature-independent constant k_0 ($\approx 2.11 \times 10^5$ s^{-1}), which is comparable to the radiative constant ($k_r = \Phi_{PL}/\tau \approx 1.65 \times 10^5$ s^{-1} in CH$_3$CN) obtained from the data collected at room temperature (Table 3). The other terms are temperature dependent; the second one is associated with the thermal redistribution between the triplet sublevels (dependent on the zero field splitting, zfs), and the third one is concerned with the population of nonradiative ^{3}MC states.

In Figure 8, both complexes **4a** and **5a** show an almost identical behavior below 200 K. In this low-temperature range only one temperature-dependent deactivation process (k_1) contributes to the reduction of the T$_1$ lifetime. Such a process is the thermal redistribution between the triplet sublevels, as suggested by the low value of the associated frequency factor ($A_1 \approx 2.6 \times 10^6$ s^{-1}, Table 7); accordingly, ΔE_1 represents the zfs between the T$_I$ and T$_{III}$ triplet substates, estimated to be around 0.06 eV for both complexes. This calculated splitting is in good agreement with reported values for similar cationic iridium(III) complexes.[44]

If the trend toward decreasing lifetimes observed for **4a** and **5a** when warming from 77 to 200 K is basically the same, this is not the case when the temperature is raised above 200 K. In fact, while the thermal population of the higher triplet sublevels still plays a predominant role for the :C^C: complex **5a** up to room temperature, for the N^C: system **4a** an additional and

very fast deactivation pathway (k_2) starts to dramatically reduce the excited-state lifetime of **4a**. The frequency factor associated with this kinetic process ($A_2 = 1.5 \times 10^{14}$ s^{-1}, Table 7) suggests that the calculated value of ΔE_2 (0.40 eV) represents the activation energy for the population of a thermally accessible nonradiative ^{3}MC excited state (Figure 9a).[53]
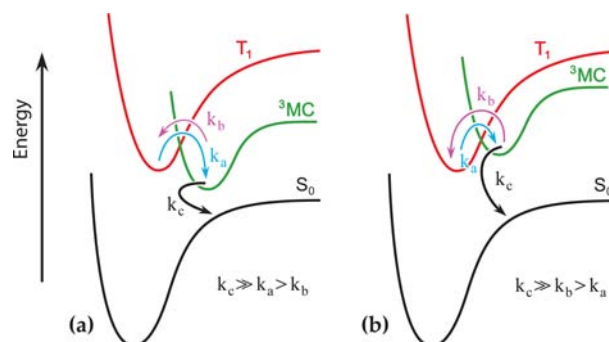

Figure 9. Potential energy curves showing the different kinetic behavior observed for **4a** (a) and **5a** (b) as representative examples of the N^C: and the :C^C: families, respectively. In both cases, (i) the position of the T$_1$ state is almost the same with respect to the S$_0$ potential energy surface (as derived from the emission spectra and the DFT calculations), and (ii) the ^{3}MC states deactivation (k_c) is fast if compared to the thermal equilibration between T$_1$ and ^{3}MC states. The main difference between the two models is the position of the ^{3}MC potential energy minimum that leads to different k_a/k_b ratios (i.e., >1 for **4a**; <1 for **5a**). The relative energy position of the curves is scaled according to the experimental and the DFT data.

Clearly, the :C^C: complex also displays a similar deactivation trend, but this is much less pronounced and starts to affect lifetime values only above 300 K. Notably, for **5a**, when compared to **4a**, the frequency factor associated with the thermal population of nonradiative ^{3}MC states is almost 10 times lower (2.1×10^{13} s^{-1}), and the activation energy barrier is higher (0.48 eV).

A rationale explaining these experimental findings can be proposed by considering in more detail the processes related to the kinetic constant k_2. In fact, the population of a higher-lying nonradiative ^{3}MC excited state is described by an activated surface crossing from the emitting T$_1$ state to a ^{3}MC level (with kinetic constant k_a), which can eventually undergo a photochemical and/or a photophysical deactivation. We term k_c the sum of the rate constants related to all the processes that deactivate ^{3}MC, with the exception of the back reaction to T$_1$ (defined as k_b). The scenario can be described by the following eq 2:

$$T_1 \underset{k_b}{\overset{k_a}{\rightleftharpoons}} {}^3MC \overset{k_c}{\rightarrow} S_0 \tag{2}$$

Table 7. Kinetic Parameters for Excited-State Decays Obtained from Temperature-Dependent Measurements in Butyronitrile Solution[a]

complex	k_0 (10^5 s^{-1})	A_1 (10^6 s^{-1})	ΔE_1 (eV)	A_2 (10^{14} s^{-1})	ΔE_2 (eV)	R^2
4a	2.11*	2.6*	0.064*	1.5 ± 0.3	0.395 ± 0.005	0.9986
5a	2.11 ± 0.04	2.6 ± 0.6	0.064 ± 0.005	0.21 ± 0.04	0.478 ± 0.006	0.9999

[a]Values are reported in a ±95% confidence interval. Some parameters in the fitting of the rate constants of **4a** (denoted by symbol*) are taken from the related fitting of **5a** due to the extremely high value of A_2 that prevents determination of much smaller parameters at lower temperatures.

In this frame, the experimental deactivation rate constant that comes into play at higher temperatures ($k_2 = A_2 \exp(-\Delta E_2 / k_B T)$) can be expressed on the basis of eq 3:

$$k_2 = k_a \frac{k_c}{k_b + k_c} \tag{3}$$

As mentioned previously, the high pre-exponential factors A_2 found for both **4a** and **5a** (Table 7) suggest that $k_c \gg k_b$; hence, the decay of ^{3}MC to S_0 is rapid if compared to the back process to T_1 and we can consider $k_2 \approx k_a$. This approximation seems to be particularly suitable for the N^C: complexes since, as determined by the DFT calculations, the minimum of the ^{3}MC state is found to be 0.30 eV lower in energy than that for the T_1 optimized state (Figure 9a), so that k_b is expected to be even lower than k_a itself. Accordingly, the k_b contribution can be neglected, and eq 2 describes a consecutive reaction having k_a as the rate-determining step. This picture is consistent with the extremely high pre-exponential factor A_2 observed for **4a** (1.5×10^{14} s^{-1}, Table 7).

On the other hand, for the :C^C: complex **5a**, the DFT calculations do not localize a low-energy ^{3}MC state. Therefore, the ^{3}MC state minimum is expected to be at higher energy with respect to the T_1 minimum, and k_b should be higher than k_a (see Figure 9b). Experimentally, we have a clue for this scenario because, in the case of **5a**, the pre-exponential factor A_2 is much smaller than it is for **4a** (2.1×10^{13} s^{-1} vs 1.5×10^{14} s^{-1}, Table 7).

CONCLUSION

We have prepared two series of charged iridium complexes based on ppy and diFppy C^N ligands. Both series use one :C^C: and four different N^C: chelators as bidentate ancillary ligands. Full photophysical characterization of the two series of complexes was performed in solution, in PMMA films, and in the solid state (as a powder). In spite of almost comparable k_r values ($\sim 1.5 \times 10^5$ s^{-1}), the N^C: complexes display k_{nr} values in solution which are about 80 times higher than those for the :C^C: analogues, pointing to the presence of additional nonradiative deactivation pathways involving thermally accessible higher-lying states. On the other hand, at 77 K, all the complexes (**1−5a,b**) show very strong phosphorescence, and both families exhibit almost identical excited-state lifetimes (~ 4 μs for complexes **1−5a**). Such findings are further rationalized by means of DFT calculations and temperature-dependent excited-state deactivation studies. In contrast to the complexes based on N^C: ancillary ligands, for which a low-lying ^{3}MC state leading to the decoordination of the pyridine ring of the N^C: ligand is found, no ^{3}MC state is localized for the :C^C: complexes. In the latter case, the high-lying ^{3}MC state is poorly accessible at room temperature, and this explains the larger values observed for the Φ_{PL} of such complexes.

Until now the emission properties of charged C^N iridium(III) complexes with carbene-based ancillary ligands were typically controlled by the main C^N ligands, in contrast to the classical approach of charged complexes bearing chemically tunable N^N ancillary ligands with low-energy π^* orbitals. However, our results demonstrate the relevant impact of the ancillary ligand on the Φ_{PL}, excited-state lifetime, and energy levels of this class of Ir(III) complexes. Most notably, as the thermal accessibility of the ^{3}MC state is crucial for the stability of the complexes, this work provides guidelines for developing efficient charged complexes with carbene-based ancillary ligands, extending the scope of this promising family of deep-blue phosphorescent charged emitters.

ASSOCIATED CONTENT

S **Supporting Information**

X-ray crystallographic data for the complexes in CIF format. X-ray single crystal structures and crystallographic data of the complexes, additional absorption and emission spectra, DFT optimized geometries, ^{1}H NMR, ^{19}F NMR, ^{31}P NMR, and HRMS spectra for selected complexes. This material is available free of charge via the Internet at http://pubs.acs.org.

AUTHOR INFORMATION

Corresponding Authors
*(N.A.) E-mail: nicola.armaroli@isof.cnr.it.
*(E.O.) E-mail: enrique.orti@uv.es.
*(E.B.) E-mail: e.baranoff@bham.ac.uk.
Notes
The authors declare no competing financial interest.

ACKNOWLEDGMENTS

REFERENCES

(1) Flamigni, L.; Barbieri, A.; Sabatini, C.; Ventura, B.; Barigelletti, F. *Top. Curr. Chem.* **2007**, *281*, 143.
(2) You, Y.; Nam, W. *Chem. Soc. Rev.* **2012**, *41*, 7061.
(3) Costa, R. D.; Ortí, E.; Bolink, H. J.; Monti, F.; Accorsi, G.; Armaroli, N. *Angew. Chem., Int. Ed.* **2012**, *51*, 8178.
(4) Hu, T.; He, L.; Duan, L.; Qiu, Y. *J. Mater. Chem.* **2012**, *22*, 4206.
(5) Lowry, M. S.; Bernhard, S. *Chem.—Eur. J.* **2006**, *12*, 7970.
(6) Holmes, R. J.; Forrest, S. R.; Sajoto, T.; Tamayo, A.; Djurovich, P. I.; Thompson, M. E.; Brooks, J.; Tung, Y. J.; D'Andrade, B. W.; Weaver, M. S.; Kwong, R. C.; Brown, J. J. *Appl. Phys. Lett.* **2005**, *87*, 243507.
(7) Yang, C.-H.; Li, S.-W.; Chi, Y.; Cheng, Y.-M.; Yeh, Y.-S.; Chou, P.-T.; Lee, G.-H.; Wang, C.-H.; Shu, C.-F. *Inorg. Chem.* **2005**, *44*, 7770.
(8) Chin, C. S.; Eum, M. S.; Kim, S. Y.; Kim, C.; Kang, S. K. *Eur. J. Inorg. Chem.* **2007**, 372.
(9) Shavaleev, N. M.; Monti, F.; Scopelliti, R.; Baschieri, A.; Sambri, L.; Armaroli, N.; Grätzel, M.; Nazeeruddin, M. K. *Organometallics* **2013**, *32*, 460.
(10) Meng, S.; Jung, I.; Feng, J.; Scopelliti, R.; Di Censo, D.; Grätzel, M.; Nazeeruddin, M. K.; Baranoff, E. *Eur. J. Inorg. Chem.* **2012**, 3209.
(11) Yang, C. H.; Beltran, J.; Lemaur, V.; Cornil, J.; Hartmann, D.; Sarfert, W.; Frohlich, R.; Bizzarri, C.; De Cola, L. *Inorg. Chem.* **2010**, *49*, 9891.
(12) Tamayo, A. B.; Garon, S.; Sajoto, T.; Djurovich, P. I.; Tsyba, I. M.; Bau, R.; Thompson, M. E. *Inorg. Chem.* **2005**, *44*, 8723.
(13) Zhao, Q.; Yu, M. X.; Shi, L. X.; Liu, S. J.; Li, C. Y.; Shi, M.; Zhou, Z. G.; Huang, C. H.; Li, F. Y. *Organometallics* **2010**, *29*, 1085.

(14) Li, J.; Djurovich, P. I.; Alleyne, B. D.; Yousufuddin, M.; Ho, N. N.; Thomas, J. C.; Peters, J. C.; Bau, R.; Thompson, M. E. *Inorg. Chem.* **2005**, *44*, 1713.

(15) Ladouceur, S.; Fortin, D.; Zysman-Colman, E. *Inorg. Chem.* **2011**, *50*, 11514.

(16) Sun, L.; Galan, A.; Ladouceur, S.; Slinker, J. D.; Zysman-Colman, E. *J. Mater. Chem.* **2011**, *21*, 18083.

(17) Parker, S. T.; Slinker, J. D.; Lowry, M. S.; Cox, M. P.; Bernhard, S.; Malliaras, G. G. *Chem. Mater.* **2005**, *17*, 3187.

(18) Beyer, B.; Ulbricht, C.; Escudero, D.; Friebe, C.; Winter, A.; González, L.; Schubert, U. S. *Organometallics* **2009**, *28*, 5478.

(19) Slinker, J. D.; Koh, C. Y.; Malliaras, G. G.; Lowry, M. S.; Bernhard, S. *Appl. Phys. Lett.* **2005**, *86*, 173506.

(20) Rothe, C.; Chiang, C. J.; Jankus, V.; Abdullah, K.; Zeng, X. S.; Jitchati, R.; Batsanov, A. S.; Bryce, M. R.; Monkman, A. P. *Adv. Funct. Mater.* **2009**, *19*, 2038.

(21) He, L.; Duan, L.; Qiao, J.; Wang, R. J.; Wei, P.; Wang, L. D.; Qiu, Y. *Adv. Funct. Mater.* **2008**, *18*, 2123.

(22) He, L.; Qiao, J.; Duan, L.; Dong, G. F.; Zhang, D. Q.; Wang, L. D.; Qiu, Y. *Adv. Funct. Mater.* **2009**, *19*, 2950.

(23) Mydlak, M.; Bizzarri, C.; Hartmann, D.; Sarfert, W.; Schmid, G.; De Cola, L. *Adv. Funct. Mater.* **2010**, *20*, 1812.

(24) Stagni, S.; Colella, S.; Palazzi, A.; Valenti, G.; Zacchini, S.; Paolucci, F.; Marcaccio, M.; Albuquerque, R. Q.; De Cola, L. *Inorg. Chem.* **2008**, *47*, 10509.

(25) Kessler, F.; Costa, R. D.; Di Censo, D.; Scopelliti, R.; Ortí, E.; Bolink, H. J.; Meier, S.; Sarfert, W.; Graetzel, M.; Nazeeruddin, M. K.; Baranoff, E. *Dalton Trans.* **2012**, *41*, 180.

(26) Zhang, F. L.; Duan, L.; Qiao, J.; Dong, G. F.; Wang, L. D.; Qiu, Y. *Org. Electron.* **2012**, *13*, 1277.

(27) Duisenberg, A. J. M.; Kroon-Batenburg, L. M. J.; Schreurs, A. M. M. *J. Appl. Crystallogr.* **2003**, *36*, 220.

(28) Blessing, R. H. *Acta Crystallogr., Sect. A: Found. Crystallogr.* **1995**, *51*, 33.

(29) Sheldrick, G. M. *Acta Crystallogr., Sect. A: Found. Crystallogr.* **2008**, *64*, 112.

(30) Crosby, G. A.; Demas, J. N. *J. Phys. Chem.* **1971**, *75*, 991.

(31) Nakamaru, K. *Bull. Chem. Soc. Jpn.* **1982**, *55*, 2697.

(32) Meech, S. R.; Phillips, D. *J. Photochem.* **1983**, *23*, 193.

(33) De Mello, J. C.; Wittmann, H. F.; Friend, R. H. *Adv. Mater.* **1997**, *9*, 230.

(34) Frisch, M. J.; Trucks, G. W.; Schlegel, H. B.; Scuseria, G. E.; Robb, M. A.; Cheeseman, J. R.; Scalmani, G.; Barone, V.; Mennucci, B.; Petersson, G. A.; Nakatsuji, H.; Caricato, M.; Li, X.; Hratchian, H. P.; Izmaylov, A. F.; Bloino, J.; Zheng, G.; Sonnenberg, J. L.; Hada, M.; Ehara, M.; Toyota, K.; Fukuda, R.; Hasegawa, J.; Ishida, M.; Nakajima, T.; Honda, Y.; Kitao, O.; Nakai, H.; Vreven, T.; Montgomery, J., J. A.; Peralta, J. E.; Ogliaro, F.; Bearpark, M.; Heyd, J. J.; Brothers, E.; Kudin, K. N.; Staroverov, V. N.; Keith, T.; Kobayashi, R.; Normand, J.; Raghavachari, K.; Rendell, A.; Burant, J. C.; Iyengar, S. S.; Tomasi, J.; Cossi, M.; Rega, N.; Millam, J. M.; Klene, M.; Knox, J. E.; Cross, J. B.; Bakken, V.; Adamo, C.; Jaramillo, J.; Gomperts, R.; Stratmann, R. E.; Yazyev, O.; Austin, A. J.; Cammi, R.; Pomelli, C.; Ochterski, J. W.; Martin, R. L.; Morokuma, K.; Zakrzewski, V. G.; Voth, G. A.; Salvador, P.; Dannenberg, J. J.; Dapprich, S.; Daniels, A. D.; Farkas, Ö.; Foresman, J. B.; Ortiz, J. V.; Cioslowski, J.; Fox, D. J. *Gaussian 09*, Revision C.01; Gaussian, Inc.: Wallingford, CT, 2010.

(35) Becke, A. D. *J. Chem. Phys.* **1993**, *98*, 5648.

(36) Lee, C. T.; Yang, W. T.; Parr, R. G. *Phys. Rev. B: Condens. Matter Mater. Phys.* **1988**, *37*, 785.

(37) Francl, M. M.; Pietro, W. J.; Hehre, W. J.; Binkley, J. S.; Gordon, M. S.; Defrees, D. J.; Pople, J. A. *J. Chem. Phys.* **1982**, *77*, 3654.

(38) Hay, P. J.; Wadt, W. R. *J. Chem. Phys.* **1985**, *82*, 299.

(39) Cramer, C. S.; Truhlar, D. G. *Solvent Effects and Chemical Reactivity*; Kluwer: Dordrecht, 1996.

(40) Tomasi, J.; Mennucci, B.; Cammi, R. *Chem. Rev.* **2005**, *105*, 2999.

(41) Tomasi, J.; Persico, M. *Chem. Rev.* **1994**, *94*, 2027.

(42) Marenich, A. V.; Cramer, C. S.; Truhlar, D. G. *J. Phys. Chem. B* **2009**, *113*, 6378.

(43) Verma, A. K.; Singh, J.; Sankar, V. K.; Chaudhary, R.; Chandra, R. *Tet. Lett.* **2007**, *48*, 4207.

(44) Costa, R. D.; Monti, F.; Accorsi, G.; Barbieri, A.; Bolink, H. J.; Ortí, E.; Armaroli, N. *Inorg. Chem.* **2011**, *50*, 7229.

(45) Dedeian, K.; Shi, J. M.; Forsythe, E.; Morton, D. C.; Zavalij, P. Y. *Inorg. Chem.* **2007**, *46*, 1603.

(46) Bolink, H. J.; Coronado, E.; Costa, R. D.; Lardies, N.; Ortí, E. *Inorg. Chem.* **2008**, *47*, 9149.

(47) De Angelis, F.; Fantacci, S.; Evans, N.; Klein, C.; Zakeeruddin, S. M.; Moser, J. E.; Kalyanasundaram, K.; Bolink, H. J.; Gratzel, M.; Nazeeruddin, M. K. *Inorg. Chem.* **2007**, *46*, 5989.

(48) Lowry, M. S.; Goldsmith, J. I.; Slinker, J. D.; Rohl, R.; Pascal, R. A.; Malliaras, G. G.; Bernhard, S. *Chem. Mater.* **2005**, *17*, 5712.

(49) Costa, R. D.; Ortí, E.; Bolink, H. J.; Graber, S.; Schaffner, S.; Neuburger, M.; Housecroft, C. E.; Constable, E. C. *Adv. Funct. Mater.* **2009**, *19*, 3456.

(50) Nozaki, K.; Takamori, K.; Nakatsugawa, Y.; Ohno, T. *Inorg. Chem.* **2006**, *45*, 6161.

(51) Tordera, D.; Delgado, M.; Ortí, E.; Bolink, H. J.; Frey, J.; Nazeeruddin, M. K.; Baranoff, E. *Chem. Mater.* **2012**, *24*, 1896.

(52) Caspar, J. V.; Meyer, T. J. *J. Am. Chem. Soc.* **1983**, *105*, 5583.

(53) Barigelletti, F.; Juris, A.; Balzani, V.; Belser, P.; von Zelewsky, A. *J. Phys. Chem.* **1987**, *91*, 1095.

10305

dx.doi.org/10.1021/ic400600d | *Inorg. Chem.* 2013, 52, 10292–10305